

Post-earthquake relaxation using a spectral element method: 2.5-D case

F. F. Pollitz

U.S. Geological Survey, Menlo Park, CA 94025, USA. E-mail: fpollitz@usgs.gov

Accepted 2014 March 24. Received 2014 February 20; in original form 2013 November 17

SUMMARY

The computation of quasi-static deformation for axisymmetric viscoelastic structures on a gravitating spherical earth is addressed using the spectral element method (SEM). A 2-D spectral element domain is defined with respect to spherical coordinates of radius and angular distance from a pole of symmetry, and 3-D viscoelastic structure is assumed to be azimuthally symmetric with respect to this pole. A point dislocation source that is periodic in azimuth is implemented with a truncated sequence of azimuthal order numbers. Viscoelasticity is limited to linear rheologies and is implemented with the correspondence principle in the Laplace transform domain. This leads to a series of decoupled 2-D problems which are solved with the SEM. Inverse Laplace transform of the independent 2-D solutions leads to the time-domain solution of the 3-D equations of quasi-static equilibrium imposed on a 2-D structure. The numerical procedure is verified through comparison with analytic solutions for finite faults embedded in a laterally homogeneous viscoelastic structure. This methodology is applicable to situations where the predominant structure varies in one horizontal direction, such as a structural contrast across (or parallel to) a long strike-slip fault.

Key words: Numerical solutions; Transient deformation; Mechanics, theory, and modelling.

1 INTRODUCTION

Calculations of quasi-static deformation play a central role in viscoelastic relaxation problems, for example, post-earthquake relaxation, post-glacial rebound and the rebound from lacustrine lake filling or draining (e.g. Bürgmann & Dresen 2008; Thatcher & Pollitz 2008; Hammond *et al.* 2009). 1-D (i.e. radially stratified) viscoelastic formulations have proven a powerful tool for interpreting time-dependent, post-earthquake crustal motions (e.g. Rundle 1980; Piersanti *et al.* 1995; Pollitz 1997; Zeng 2001; Fernandez & Rundle 2004; Freed & Bürgmann 2004; Wang *et al.* 2006) and the time-dependent response to lake filling (Kaufmann & Amelung 2000; Luttrell *et al.* 2007; Brothers *et al.* 2011) and draining (Bills *et al.* 1994). However, these models encounter limitations in tectonically complicated environments where strong lateral variations in elastic parameters or viscosity may exist, for example, descending slabs at subduction zones or around faults that divide different geological terranes.

It is advantageous to include lateral variations in viscoelastic structure in numerical models. Hu & Wang (2012) and Pollitz *et al.* (2008) have found such models useful for interpreting motions following large megathrust earthquakes. Malservisi *et al.* (2001), Hearn *et al.* (2009), Ryder *et al.* (2011) and Pollitz *et al.* (2012) find that such models are necessary to account for motions around a major fault following large strike-slip earthquakes. 3-D numerical models based on a Fourier domain elastic Green's function (Barbot

& Fialko 2010a,b) and the finite element method (e.g. Melosh & Raefsky 1980; Zhong *et al.* 2003; Freed *et al.* 2007; Parker *et al.* 2008; Hearn *et al.* 2009; Aagaard *et al.* 2013) are well suited to address problems with laterally variable viscoelastic structure. 3-D finite element models for quasi-static deformation require the computation of the inverse of a banded matrix and, therefore, have potentially large memory demands. Their spatial accuracy depends on the basis functions and numerical integration scheme. 2-D models, or models involving the solution of a series of 2-D models, have much smaller demands on memory. Also, the spectral element method (SEM), which has found wide applications in propagating wave seismology (e.g. Komatitsch & Vilotte 1998; Komatitsch & Tromp 1999, 2002a), is based on Gauss-Legendre-Lobatto (GLL) quadrature, has high spatial accuracy and is well suited for quasi-static deformation, as well as seismic wave propagation. Al-Attar & Tromp (2014) apply SEM to the quasi-static deformation problem in order to derive Frechet sensitivity kernels with respect to viscoelastic parameters for a linear Maxwell rheology, and they demonstrate its utility for spherically symmetric models using a 1-D SEM.

Both time domain and Laplace transform domain approaches are feasible for the solving of quasi-static deformation problem. A time domain approach is an efficient and direct way to obtain the solution. The chief advantage of the Laplace transform domain approach that we shall employ is that even a complicated linear rheology may be implemented with ease, as the stress-strain relation for a linear rheology is expressible in a compact form, that is,

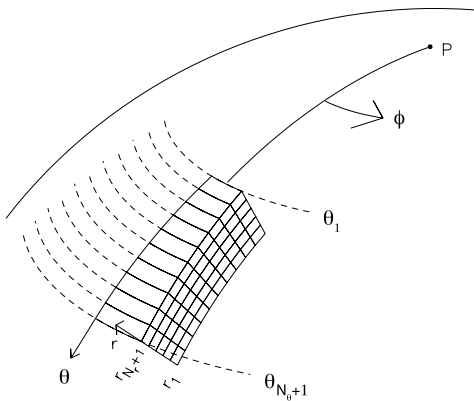


Figure 1. Geometry of model domain in 2.5-D. Viscoelastic structure is assumed symmetric with respect to a symmetry pole P , that is, it does not vary with ϕ , but may vary with θ and r . There are N_θ and N_r divisions of the model domain in the θ and r coordinates, respectively.

through the complex compliance (Bland 1960). A disadvantage is that a non-linear (e.g. stress-dependent) rheology is more difficult to implement. An iterative approach can be devised to solve for quasi-static deformation for a non-linear rheology in the Laplace transform domain, but deformation in this case would be more straightforward to obtain with a time domain approach.

In this study, we present a 2.5-D method for calculating quasi-static deformation on a laterally variable viscoelastic structure in a spherical earth geometry. The viscoelasic structure is 2-D (azimuthally symmetric about a given Euler pole), and it is implemented in the Laplace transform domain for a prescribed linear rheology. For a given azimuthal order number m , the equations of quasi-static equilibrium decouple into a series of 2-D equations, which may be solved separately in terms of both m and the Laplace transform parameter. Summation over azimuthal order number combined with inverse Laplace transform yields time-dependent quasi-static deformation. We describe the implementation of SEM for a seismic point source, noting the method could be readily extended to the problem of surface loading. Comparison with analytic solutions for finite earthquake sources on laterally homogeneous models is used to verify this application of the SEM.

2 SEM APPLIED TO 2.5-D QUASI-STATIC DEFORMATION

We follow Komatitsch & Tromp (1999) in implementing the SEM. We begin with the equations of quasi-static equilibrium in a spherical geometry. For the quasi-static problem, in contrast to seismic wave propagation, the inertial terms of the momentum equation are neglected. With the 2.5-D system we assume symmetry of the viscoelastic structure with respect to a pole of symmetry, and it consequently involves the solution of a series of 2-D systems. The strong form of the equations of motion are converted to the weak form, then discretized using Lagrange basis functions on GLL quadrature points within 2-D cells. A sum over discretized wave numbers (i.e. azimuthal order numbers in the spherical coordinate of longitude) is used to handle the third dimension. With specification of a moment tensor point force, this leads to a linear system of equations. The model domain is designed to avoid the pole of symmetry itself. That distinguishes the present method from that of Nissen-Meyer *et al.* (2007) in the seismic wave propagation case, in which the model domain includes the pole of symmetry and the source is placed along the symmetry axis.

We work in the Laplace transform domain in order to implement linear viscoelasticity using a correspondence principle, with the consequence that the method requires calculating the inverse of a banded matrix for every Laplace transform parameter and azimuthal order number. Rather than present a treatment for general quadrilateral elements, which is accomplished by introducing the Jacobian of the element shape functions, we choose the simplest possible form for elements in a spherical geometry, that is, successive angular sections of a vertical slice through a sphere, each section bounded by upper and lower segments of constant curvature. Sphericity is then realized by using explicit forms of the stress tensor and differential operators in a spherical geometry.

2.1 Equations of quasi-static equilibrium

We work in a $r - \theta - \phi$ spherical coordinate system. A 2-D spectral element domain is defined with respect to spherical coordinates of radius r and angular distance θ from a pole of symmetry P (Fig. 1). Laterally variable 3-D viscoelastic structure depends only upon r and θ , that is, it is azimuthally symmetric. A seismic point source

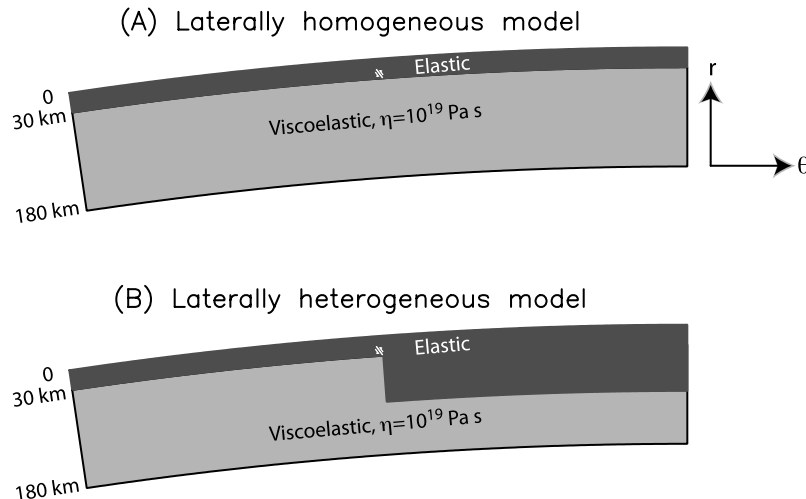


Figure 2. Sketches of the viscoelastic structures used in the examples, shown in an $r - \theta$ cross-section. (a) In the laterally homogeneous structure, the elastic layer thickness is uniformly 30 km. (b) In the laterally homogeneous structure, the elastic thickness has a sharp transition from 30 to 100 km. In both sketches, the approximate location of the finite sources used in the examples is shown.

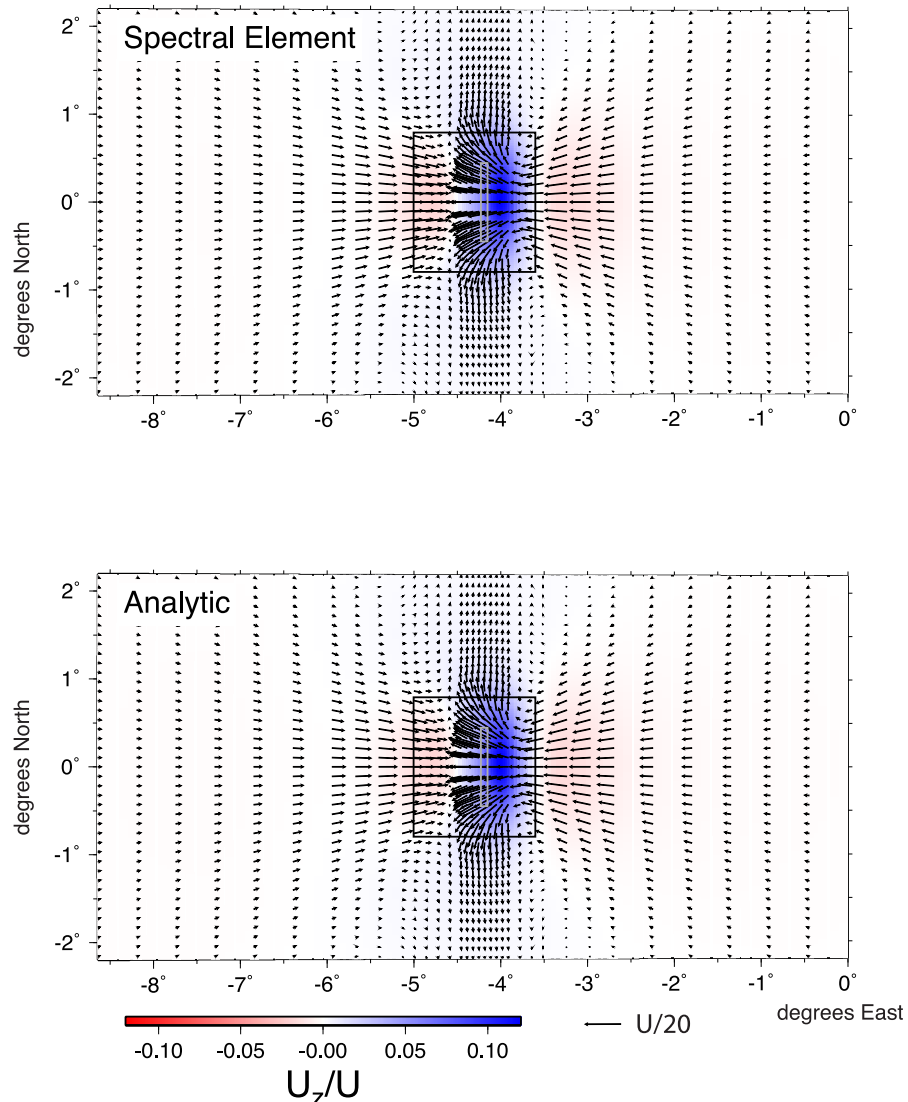


Figure 3. Horizontal displacements (arrows) and vertical displacements (colour shading) for post-thrusting relaxation on the fault plane indicated with the white rectangle. These are cumulative displacements up to 5τ years following the slip event, where τ is the material relaxation time of the ductile substrate. The colour scale indicates the ratio of vertical displacement U_z to fault slip U . In this and similar figures, displacements are shown at the GLL points subsampled by a factor of 6. Black rectangle indicates the area plotted in Fig. 4.

is implemented with an assumed periodicity in longitude ϕ with respect to P . The computational domain occupies a vertical slice bounded by a spherical shell at depth, the free surface, and vertical surfaces at two given angular distances from P .

It is convenient to work in the Laplace transform domain. The Laplace transform of a function $f(t)$ with independent variable s is

$$L[f(t)] = \int_0^\infty f(t) \exp(-st) dt. \quad (1)$$

We assume a linear viscoelastic stress-strain relation, which permits the governing equations to be expressed in terms of s -dependent elastic parameters. Let $\mathbf{u}(\mathbf{r}; s)$ be a quasi-static displacement field and $\boldsymbol{\sigma}(\mathbf{r}; s)$ the corresponding stress tensor in the Laplace transform domain. We shall assume for simplicity that the earth model consists of welded elastic and viscoelastic layers between some lower boundary and earth's surface.

On a slowly rotating ellipsoidal reference model with density $\rho(\mathbf{r})$, the reference gravitational potential Φ is given by

$$\nabla^2 \Phi(\mathbf{r}) = 4\pi G\rho(r), \quad (2)$$

where G is the gravitational constant. Following Komatitsch & Tromp (2002b), we shall neglect non-hydrostatic pre-stress and assume that the earth is in hydrostatic equilibrium. Defining ψ as the centrifugal potential, this implies that level surfaces of density ρ and geopotential $\Phi + \psi$ must coincide, for example, eq. (3.256) of Dahlen & Tromp (1998)

$$\nabla \rho \times \nabla(\Phi + \psi) = \mathbf{0}. \quad (3)$$

The gravitational acceleration vector is given by

$$\mathbf{g} = -\nabla(\Phi + \psi). \quad (4)$$

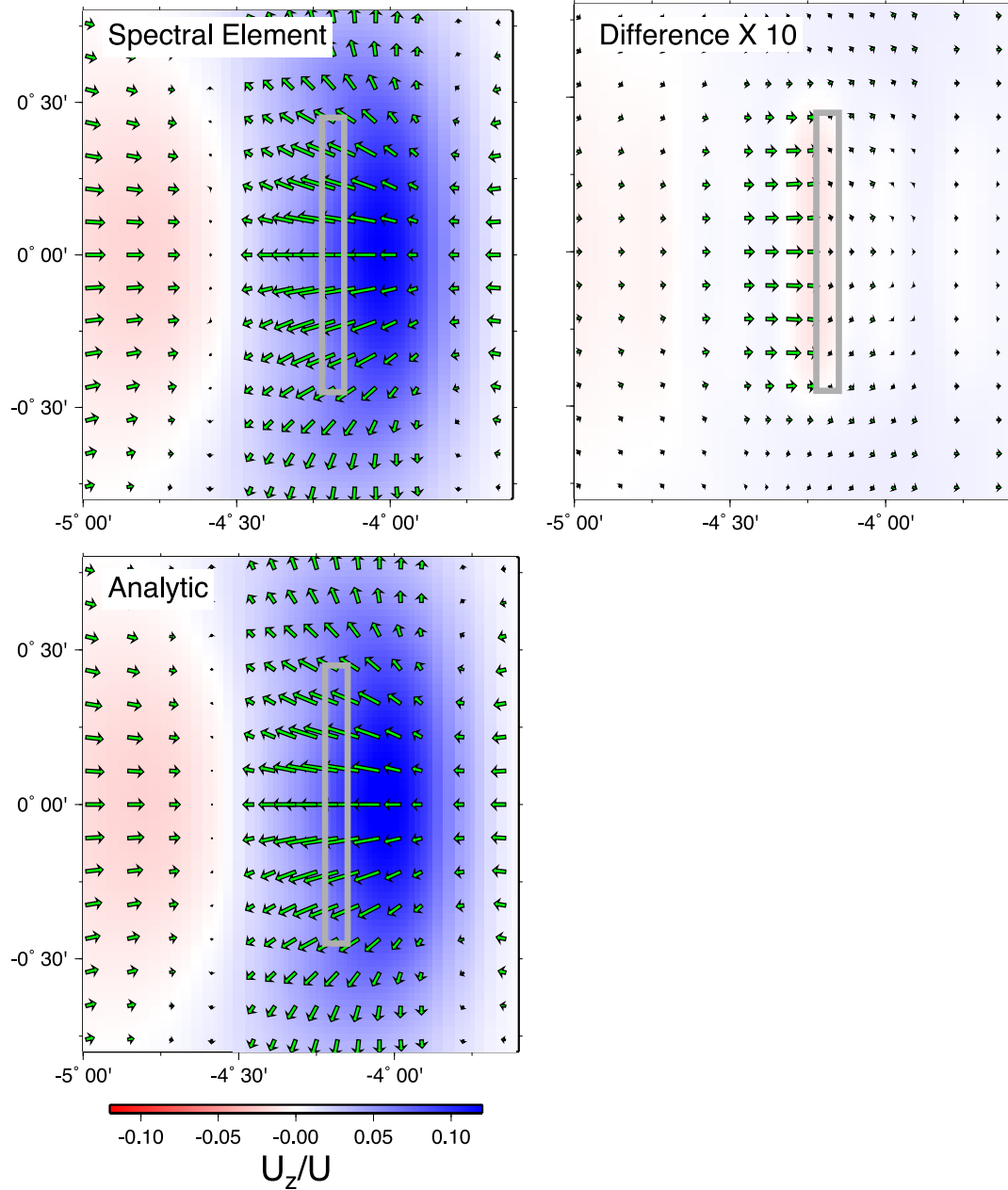


Figure 4. Close-up view of the post-thrusting motions shown in Fig. 3. Right-hand plot shows difference between SEM and analytic displacement fields.

As noted by Komatitsch & Tromp (2002b), the neglect of earth's ellipticity is a good approximation for intended applications, in which case

$$\mathbf{g} = -g_0(r)\hat{\mathbf{r}}, \quad (5)$$

where $g_0(r) = \partial_r \Phi_0(\mathbf{r})$ is the gravitational acceleration of a spherically symmetric non-rotating model with density $\rho_0(r)$ and gravitational potential

$$\nabla^2 \Phi_0(\mathbf{r}) = 4\pi G \rho_0(r). \quad (6)$$

The equations of quasi-static equilibrium for a distributed body force $\mathbf{f}(\mathbf{r}; s)$ are

$$-\rho(\mathbf{r}) \nabla \Phi_0(r) + \nabla [\rho(\mathbf{r}) \mathbf{u}(\mathbf{r}; s) \cdot \mathbf{g}] - \nabla \cdot [\rho(\mathbf{r}) \mathbf{u}(\mathbf{r}; s)] \mathbf{g} + \nabla \cdot \boldsymbol{\sigma}(\mathbf{r}; s) + \mathbf{f}(\mathbf{r}; s) = \mathbf{0}, \quad (7)$$

$$\boldsymbol{\sigma}(\mathbf{r}; s) = \mathbf{c}(\mathbf{r}; s) : \nabla \mathbf{u}(\mathbf{r}; s), \quad (8)$$

$$\nabla^2 \Phi_1(\mathbf{r}) = -4\pi G \nabla \cdot [\rho(\mathbf{r}) \mathbf{u}(\mathbf{r}; s)], \quad (9)$$

where ρ is density, Φ_1 is perturbed gravitational potential and \mathbf{c} is the elastic tensor. Eqs (5) through (9) are equivalent to eqs (3.1), (3.4), (3.46), (3.96), (3.259) and (3.260) of Dahlen & Tromp (1998) without the inertial and rotational terms.

It is feasible for most applications of post-seismic relaxation to include coupling of elastic deformation with the reference gravity field, that is, that on a spherically symmetric model, and to ignore the coupling of elastic deformation with the Eulerian perturbation in the gravitational potential. This approximation, sometimes referred to as Cowling's approximation (Dahlen & Tromp 1998), was first advocated by Rundle (1981) for post-seismic relaxation calculations

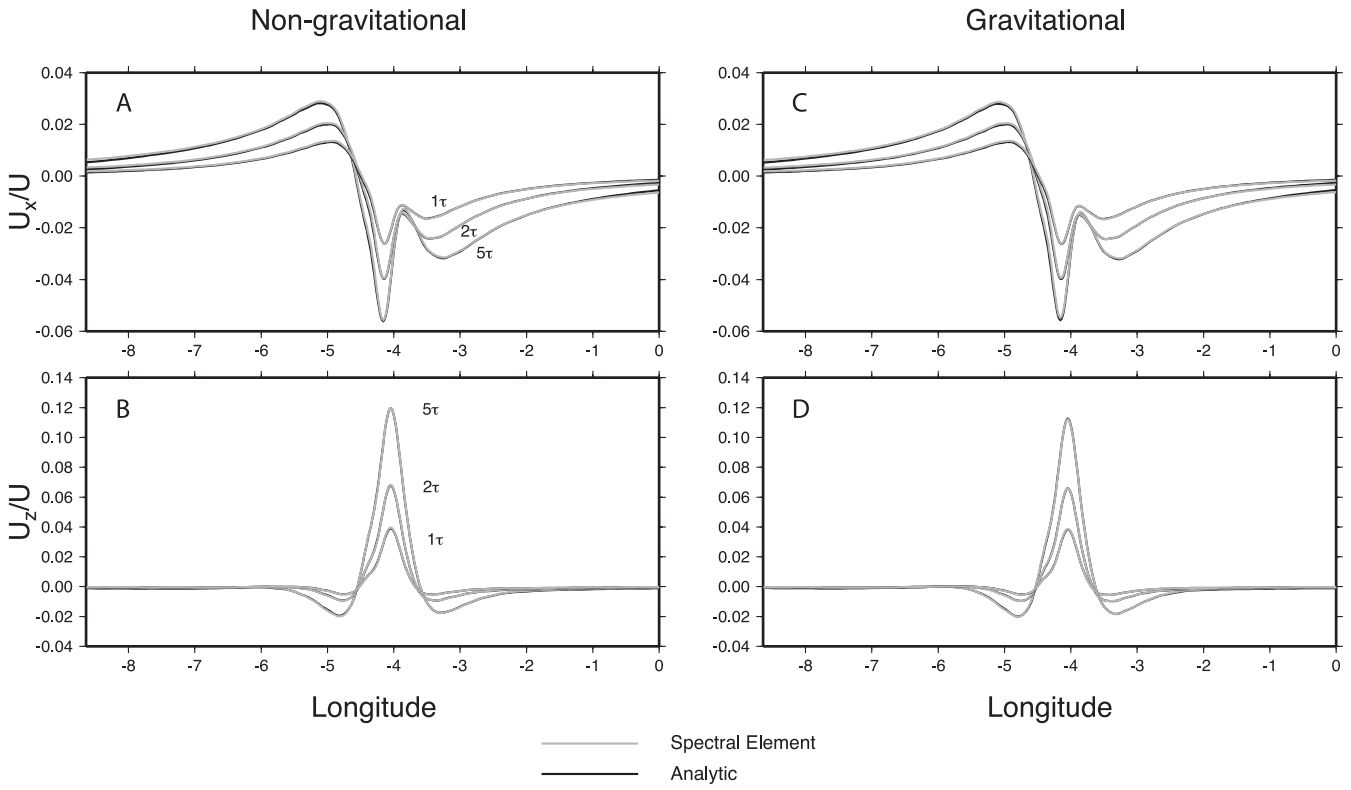


Figure 5. Ratio of horizontal displacement U_x (a, c) and vertical displacement U_z (b, d) to fault slip U for post-thrusting displacements at times 1τ , 2τ and 5τ along the equator of the area shown in Fig. 3. Non-gravitational displacements from the spectral element and analytic methods are compared in (a, b), and gravitational displacements in (c, d).

and justified by Pollitz (1997) using a scaling analysis. The approximation on a spherically symmetric model has been tested against the solution on a self-gravitating earth by Pollitz *et al.* (2006) on a regional scale. Adopting this approximation here, eq. (7) becomes

$$\nabla [\rho(\mathbf{r}) \mathbf{u}(\mathbf{r}; s) \cdot \mathbf{g}] - \nabla \cdot [\rho(\mathbf{r}) \mathbf{u}(\mathbf{r}; s)] \mathbf{g} + \nabla \cdot \boldsymbol{\sigma}(\mathbf{r}; s) + \mathbf{f}(\mathbf{r}; s) = \mathbf{0}. \quad (10)$$

Eqs (8) through (10) are to be solved subject to $\hat{\mathbf{r}} \cdot \boldsymbol{\sigma}$ at earth's surface and appropriate boundary conditions at an interior spherical shell and at the lateral edges of the model domain. At the interior spherical shell we choose vanishing displacement $\mathbf{u} = \mathbf{0}$, and at the lateral edges we choose Robin boundary conditions that honour the expected inverse dependence of displacement with lateral distance from the source (see Section 4.1).

Using eq. (3), we may rewrite eq. (10) in a form which does not involve the gradient of ρ .

$$\rho(\mathbf{r}) \nabla [\mathbf{u}(\mathbf{r}; s) \cdot \mathbf{g}] - \rho(\mathbf{r}) [\nabla \cdot \mathbf{u}(\mathbf{r}; s)] \mathbf{g} + \nabla \cdot \boldsymbol{\sigma}(\mathbf{r}; s) + \mathbf{f}(\mathbf{r}; s) = \mathbf{0}. \quad (11)$$

For a scalar function $w(r, \theta)$ within element Γ , which may be a Lagrange interpolation polynomial (Appendix A), and an azimuthal order number m , we define test functions

$$\mathbf{w}_j(\mathbf{r}) = \frac{1}{2\pi} w(r, \theta) e^{-im\phi} \begin{cases} \hat{\theta}, & \text{if } j = 1 \\ \hat{\phi}, & \text{if } j = 2 \\ \hat{\mathbf{r}}, & \text{if } j = 3 \end{cases} \quad (12)$$

We take the vector product of $\mathbf{w}_j(\mathbf{r})$ with eq. (11) and integrate over a volume V , the annulus swept out by the area Γ over azimuth range

from 0 to 2π about the pole of symmetry:

$$\int_V \mathbf{w}_j(\mathbf{r}) \cdot \{\rho(\mathbf{r}) \nabla [\mathbf{u}(\mathbf{r}; s) \cdot \mathbf{g}] - \rho(\mathbf{r}) \nabla \cdot [\mathbf{u}(\mathbf{r}; s)] \mathbf{g}\} d^3\mathbf{r} + \int_V \mathbf{w}_j(\mathbf{r}) \cdot [\nabla \cdot \boldsymbol{\sigma}(\mathbf{r}; s)] d^3\mathbf{r} = - \int_V \mathbf{w}_j(\mathbf{r}) \cdot \mathbf{f}(\mathbf{r}; s) d^3\mathbf{r}. \quad (13)$$

We obtain the weak form of eq. (13) by applying the divergence theorem to the $\nabla \cdot \boldsymbol{\sigma}$ term. This yields

$$\int_V \mathbf{w}_j(\mathbf{r}) \cdot \{\rho(\mathbf{r}) \nabla [\mathbf{u}(\mathbf{r}; s) \cdot \mathbf{g}] - \rho(\mathbf{r}) [\nabla \cdot \mathbf{u}(\mathbf{r}; s)] \mathbf{g}\} d^3\mathbf{r} + \int_{\partial V} \hat{\mathbf{n}} \cdot \boldsymbol{\sigma}(\mathbf{r}; s) \cdot \mathbf{w}_j(\mathbf{r}) d^2\mathbf{r} - \int_V \nabla \mathbf{w}_j(\mathbf{r}) : \boldsymbol{\sigma}(\mathbf{r}; s) d^3\mathbf{r} = - \int_V \mathbf{w}_j(\mathbf{r}) \cdot \mathbf{f}(\mathbf{r}; s) d^3\mathbf{r}, \quad (14)$$

where ∂V is a closed surface around the global model domain and $\hat{\mathbf{n}}$ is the outward-pointing unit vector perpendicular to the surface.

Note that it is possible to obtain the weak form for the gravitational terms as well (Komatitsch & Tromp 2002b). This would be done by reverting to eq. (10) and using the relations

$$\nabla [\rho \mathbf{u} \cdot \mathbf{g}] = \nabla \cdot [\rho (\mathbf{u} \cdot \mathbf{g}) \mathbf{I}], \quad (15)$$

$$\nabla \cdot (\rho \mathbf{u}) \mathbf{g} = \nabla \cdot (\rho \mathbf{u} \mathbf{g}) - \rho \mathbf{u} \cdot \nabla \mathbf{g}, \quad (16)$$

in order to rewrite the gravitational terms in terms of the divergence operator. In this study, we retain the strong form of the gravitational terms by employing eq. (14), but the approaches taken here and in Komatitsch & Tromp (2002b) are equivalent.

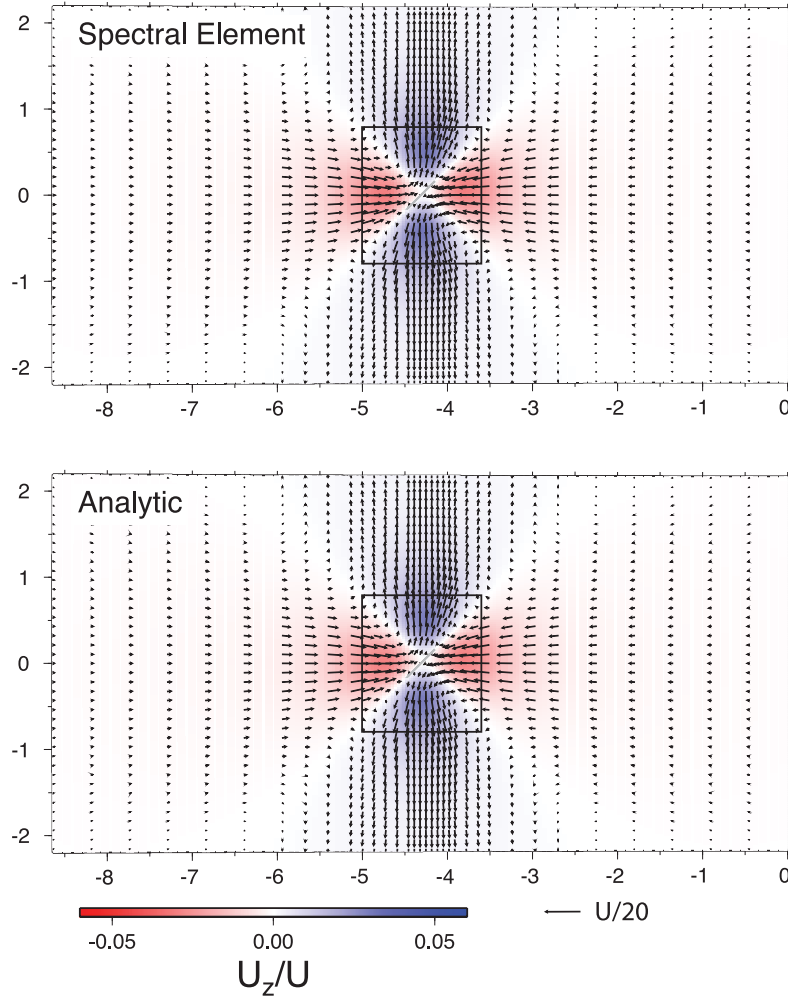


Figure 6. Horizontal displacements (arrows) and vertical displacements (colour shading) for relaxation following strike-slip faulting on the fault plane indicated with the white rectangle. These are cumulative displacements up to 5τ yr following the slip event, where τ is the material relaxation time of the ductile substrate. The colour scale indicates the ratio of vertical displacement U_z to fault slip U . Black rectangle indicates the area plotted in Fig. 7.

2.2 Model discretization

A 2-D model domain is defined in terms of radius r and angular distance θ from a fixed pole P . We define a rectangular array of elements with vertices $\{(r_k, \theta_l) | k = 1, \dots, N_r + 1, l = 1, \dots, N_\theta + 1\}$ (Fig. 1). Letting Γ denote element kl ($1 \leq k \leq N_r, 1 \leq l \leq N_\theta$), we define element dimensions $\Delta r^\Gamma = r_{k+1} - r_k$ and $\Delta \theta^\Gamma = \theta_{l+1} - \theta_l$.

Each element is discretized with GLL nodes (x_γ, x_v) of order N which are identical to the GLL quadrature points defined in Appendix A. In each spatial dimension, there are $N - 1$ interior points and one at each endpoint, that is, $x_0 = -1$ and $x_N = 1$. In element Γ , the local nodes are denoted (x_γ, x_v) and global nodes denoted $\mathbf{r}_{\gamma v}$. The latter correspond to elemental coordinate x_v ($v = 0, \dots, N$) with global radius

$$r_{\gamma v} = \frac{r_k + r_{k+1}}{2} + x_v \frac{\Delta r^\Gamma}{2} \quad (17)$$

and elemental coordinate x_γ ($\gamma = 0, \dots, N$) with global angular distance

$$\theta_{\gamma v} = \frac{\theta_l + \theta_{l+1}}{2} + x_\gamma \frac{\Delta \theta^\Gamma}{2}. \quad (18)$$

A general mapping of local to global coordinates in element Γ is

$$\begin{aligned} r &= \frac{r_k + r_{k+1}}{2} + z(r, \theta) \frac{\Delta r^\Gamma}{2} & (-1 \leq z(r, \theta) \leq 1) \\ \theta &= \frac{\theta_l + \theta_{l+1}}{2} + x(r, \theta) \frac{\Delta \theta^\Gamma}{2} & (-1 \leq x(r, \theta) \leq 1). \end{aligned} \quad (19)$$

In the Laplace transform domain, let the local 3-D displacement field be expanded as

$$\begin{aligned} \mathbf{u}(r, \theta, \phi; s) &= \sum_{m=-\infty}^{\infty} \sum_{\alpha=0}^N \sum_{\beta=0}^N \left[a_{\alpha\beta}^m(s) \psi_{\alpha\beta}(x, z) \hat{\theta} \right. \\ &\quad \left. + b_{\alpha\beta}^m(s) \psi_{\alpha\beta}(x, z) \hat{\phi} + c_{\alpha\beta}^m(s) \psi_{\alpha\beta}(x, z) \hat{\mathbf{r}} \right] e^{im\phi}, \end{aligned} \quad (20)$$

where x and z are related to θ and r , respectively, through eq. (19), and the $\psi_{\alpha\beta}$ are GLL basis functions defined in Appendix A. At the 2-D GLL nodes, the property of the basis functions given by eq. (A11) means that the displacement field at points $(r_{\gamma v}, \theta_{\gamma v})$ and arbitrary ϕ is given by

$$\mathbf{u}(r_{\gamma v}, \theta_{\gamma v}, \phi; s) = \sum_{m=-\infty}^{\infty} \left[a_{\gamma v}^m(s) \hat{\theta} + b_{\gamma v}^m(s) \hat{\phi} + c_{\gamma v}^m(s) \hat{\mathbf{r}} \right] e^{im\phi}. \quad (21)$$

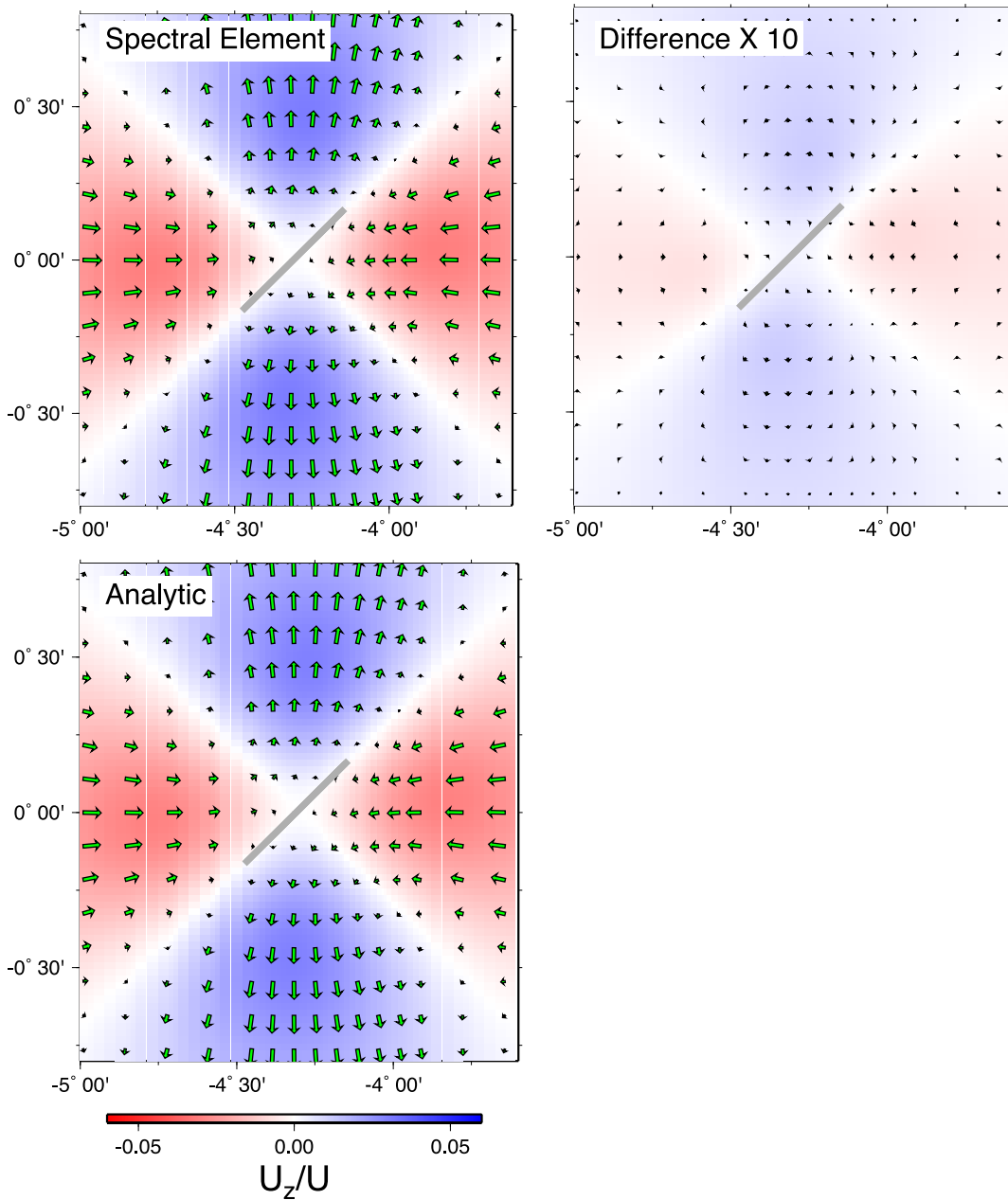


Figure 7. Close-up view of the motions following strike-slip faulting shown in Fig. 6. Right-hand plot shows difference between SEM and analytic displacement fields.

The discretized equations are obtained by substituting eq. (20) into eq. (14) and applying the 2-D integration rule (eq. A14). Evaluation of these integrals decouples into separate systems of simultaneous equations, one system for each azimuthal order number m . Each system is of the form

$$\mathbf{K}\mathbf{U} = \mathbf{F}, \quad (22)$$

where the vector of unknowns \mathbf{U} contains the $3 \times (NN_r + 1) \times (NN_\theta + 1)$ expansion coefficients of the displacement components ($a_{\alpha\beta}^m$, $b_{\alpha\beta}^m$ and $c_{\alpha\beta}^m$), three for each of the $(NN_r + 1) \times (NN_\theta + 1)$ nodes of the global grid. Each row of \mathbf{K} and \mathbf{F} corresponds to a different test function \mathbf{w}_j . The source vector \mathbf{F} for a moment tensor source and stiffness matrix \mathbf{K} are evaluated in Appendices B and C, respectively.

Note that the ϕ integral in eq. (C4) is non-zero only for displacement expansion coefficients $a_{\alpha\beta}^m$, $b_{\alpha\beta}^m$ and $c_{\alpha\beta}^m$ (i.e. displacement coefficients corresponding to the same azimuthal order number m as the test function), so that the determination of the expansion coefficients in eq. (20) decouples into the solution of a series of solutions of 2-D problems of the form $\mathbf{K}\mathbf{U} = \mathbf{F}$, with \mathbf{F} given by eq. (B6), one for each azimuthal order number m .

3 NUMERICAL IMPLEMENTATION

The Laplace-transformed displacement field at the GLL nodes are evaluated with eq. (21). The expansion coefficients of the displacement field $a_{\alpha\beta}^m$, $b_{\alpha\beta}^m$ and $c_{\alpha\beta}^m$ need be computed only for m that are integer multiples of M , the number of sources distributed uniformly

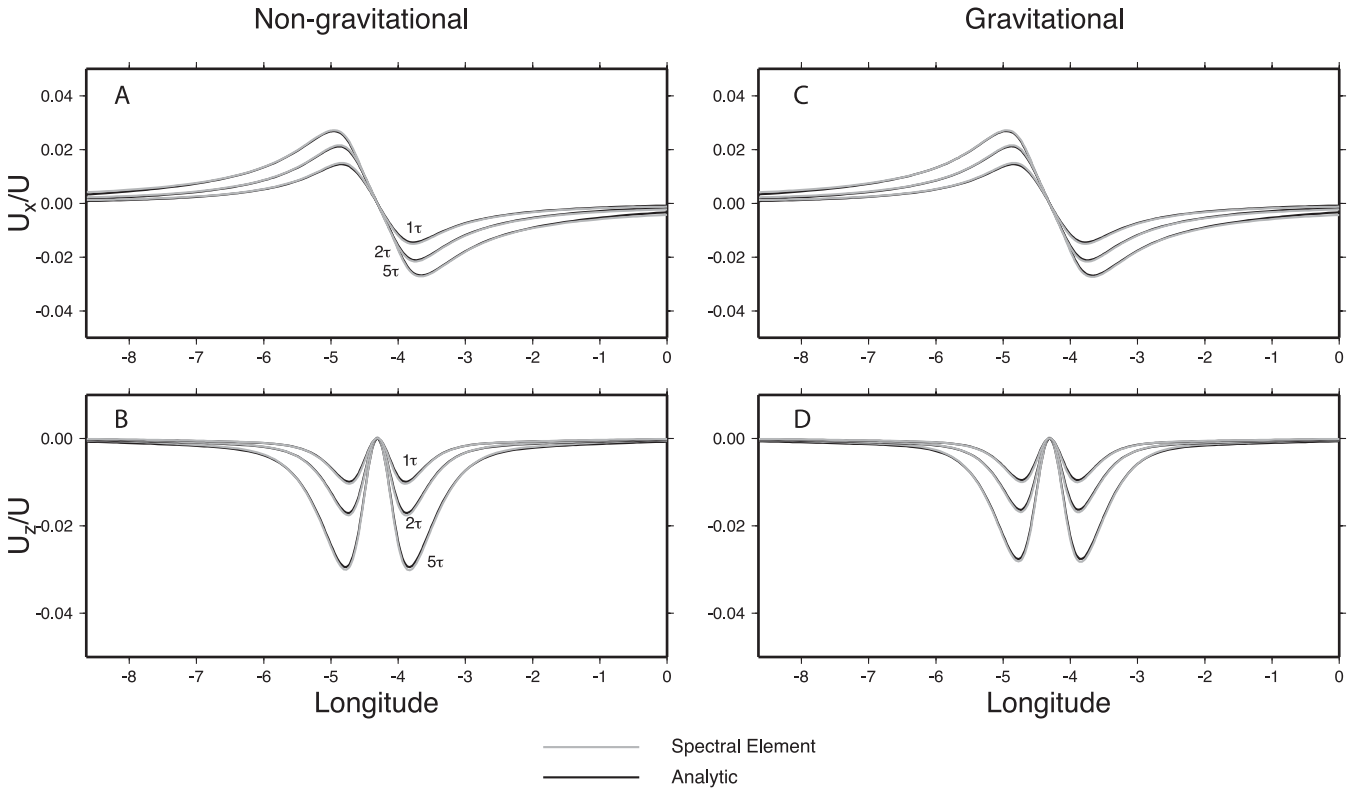


Figure 8. Ratio of horizontal displacement U_x (a, c) and vertical displacement U_z (b, d) to fault slip U for displacements following strike-slip faulting at times 1τ , 2τ and 5τ along the equator of the area shown in Fig. 6. Non-gravitational displacements from the spectral element and analytic methods are compared in (a, b), and gravitational displacements in (c, d).

in ϕ along the small circle $r = r_0$, $\theta = \theta_0$. Computational speed is thus increased by a factor of M , with the disadvantage that the displacement field in the vicinity of one of the sources will contain a small contribution from the other fictitious sources, so the displacements are accurate only out to an azimuthal distance that is a fraction of the distance between adjacent sources. The expansion must also be truncated at $|m|$ below a certain maximum value m_{\max} . If the minimum desired wavelength of the displacement field is λ_{\min} , then $m_{\max} \approx 2\pi R/\lambda_{\min}$, where R is earth's radius.

The computation speed may be further increased by a factor of 2 by taking advantage of the symmetries among the expansion coefficients $a_{\alpha\beta}^m$, $b_{\alpha\beta}^m$ and $c_{\alpha\beta}^m$. This is described in Appendix D.

For each azimuthal order number m and Laplace transform parameter s , eq. (22) is solved for the unknown expansion coefficients $a_{\alpha\beta}^m$, $b_{\alpha\beta}^m$ and $c_{\alpha\beta}^m$ of the displacement field in the Laplace transform domain. Eq. (21) truncated at $|m| < m_{\max}$ is then used to obtain Laplace-transformed displacements. In order to calculate time-dependent displacements, we follow a strategy prescribed by Pollitz (2003b) for obtaining the inverse Laplace transform. It is the Prony series solution described by Rundle (1982) and differs from Rundle's implementation only in the choice of sample points. We begin with an *a priori* estimate of the smallest material relaxation time present in the viscoelastic model. Let s_{\max} denote the reciprocal of this relaxation time. The value of s_{\max} for a specific earth model equals the reciprocal of the minimum inverse material decay time, that is, the ratio of viscosity to rigidity. We then choose a set of 12

sample points $s = s_n$ in the Laplace transform domain, determined empirically by Pollitz (2003b)

$$s_n = \frac{s_{\max}}{5.6} - 0.055(n-1)s_{\max} + [0.11(n-1)s_{\max}]i. \quad (23)$$

At these sample points we obtain the expansion coefficients and hence $\mathbf{u}(r, \theta, \phi; s_n)$ through eq. (20). We then use a collocation technique to represent the time-dependent displacement in terms of a small number of poles. To represent a function $u(s)$ which possesses simple poles between $s = 0$ and $s = -s_{\max}$ we employ an expansion using 7 inverse relaxation times:

$$u(s) = \frac{B_0}{s} + \sum_{j=1}^7 \frac{B_j}{s(s + \tau_j)}, \quad (24)$$

where B_0 is the static displacement and the B_j are coefficients of exponentially decaying signals characterizing the post-earthquake relaxation, the decay times τ_j taking the values $2s_{\max}$, s_{\max} , $s_{\max}/2$, $s_{\max}/5$, $s_{\max}/10$, $s_{\max}/100$ and $s_{\max}/500$. In the time domain,

$$u(t) = B_0 H(t) + \sum_{j=1}^7 B_j \tau_j^{-1} (1 - e^{-\tau_j t}). \quad (25)$$

Using the sample points prescribed by eq. (23), Pollitz (2003b) found that an exponentially decaying test function with a time constant of τ could be recovered with small error up to times $\sim 150\tau$; the same is true for a sum of exponentially decaying signals, each

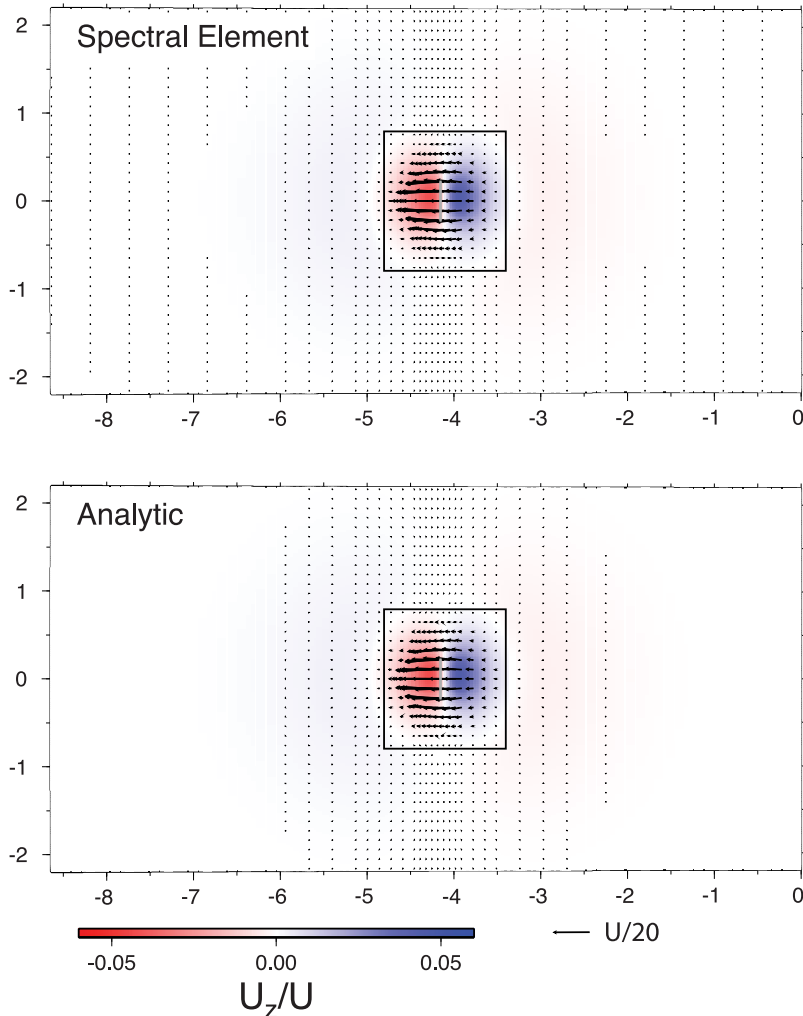


Figure 9. Horizontal displacements (arrows) and vertical displacements (colour shading) for relaxation following dip-slip faulting on the fault plane indicated with the white rectangle. These are cumulative displacements up to 5τ yr following the slip event, where τ is the material relaxation time of the ductile substrate. The colour scale indicates the ratio of vertical displacement U_z to fault slip U . Black rectangle indicates the area plotted in Fig. 10.

with an exponential time constant greater than a certain minimum, as is expected to be the case for the displacement fields considered here. The procedure described above may be applied to the set of s -dependent displacement fields $\{\mathbf{u}(r, \theta, \phi; s)|_{s=s_n}, n = 1, \dots, 12\}$ to obtain the time-dependent displacement field $\mathbf{u}(r, \theta, \phi; t)$.

The accuracy of eq. (25) for a sum of decaying exponentials is verified by comparisons between the Prony series and exact solutions presented in Rundle (1982) and Pollitz (2003b) and by comparisons in the next section between time-dependent displacements calculated by SEM and an analytic sum. The latter consists of viscoelastic normal modes described by thousands of decaying exponentials, each satisfying the condition that the employed s_{\max} is greater than the associated inverse relaxation time of all viscoelastic normal modes.

4 VERIFICATION

4.1 Setup of comparisons

We construct a model domain of dimensions 0.14172 radians (8.12 degrees) in θ and 180 km in r (Fig. 2). This domain is uniquely defined in geographic coordinates on the unit sphere by supposing

that the pole of symmetry P lies at geographic coordinates (colatitude, longitude) = $(\pi/2, \pi/2)$, the arc $\phi = 0$ coincides with the equator and along this arc $\theta = \pi/2$ and $\theta = \pi/2 + 0.14172$ correspond to geographic coordinates $(\pi/2, 0)$ and $(\pi/2, -0.14172)$, respectively. Thus, P is 90° away from the nearest edge of the model domain.

A laterally homogeneous viscoelastic model is defined with uniform elastic parameters $\kappa_0 = \lambda_0 + (2/3)\mu_0 = 50$ GPa, $\mu_0 = 30$ GPa, a purely elastic layer in the upper 30 km (viscosity $\eta = \infty$), and a Maxwell viscoelastic layer between 30 and 180 km with viscosity $\eta = 10^{19}$ Pa s (Fig. 2a). Using the correspondence principle (e.g. Segall 2010), this translates into a position and s -dependent shear modulus of

$$\mu(r, \theta; s) = \frac{\mu_0 s}{s + \mu_0/\eta}, \quad (26)$$

where η depends only on r . We assume that bulk modulus does not relax, so that

$$\lambda(r, \theta; s) = \kappa_0 - \frac{2}{3}\mu(r, \theta; s). \quad (27)$$

The size of each 2-D GLL element is guided by the minimum wavelength of deformation expected at a chosen depth. The

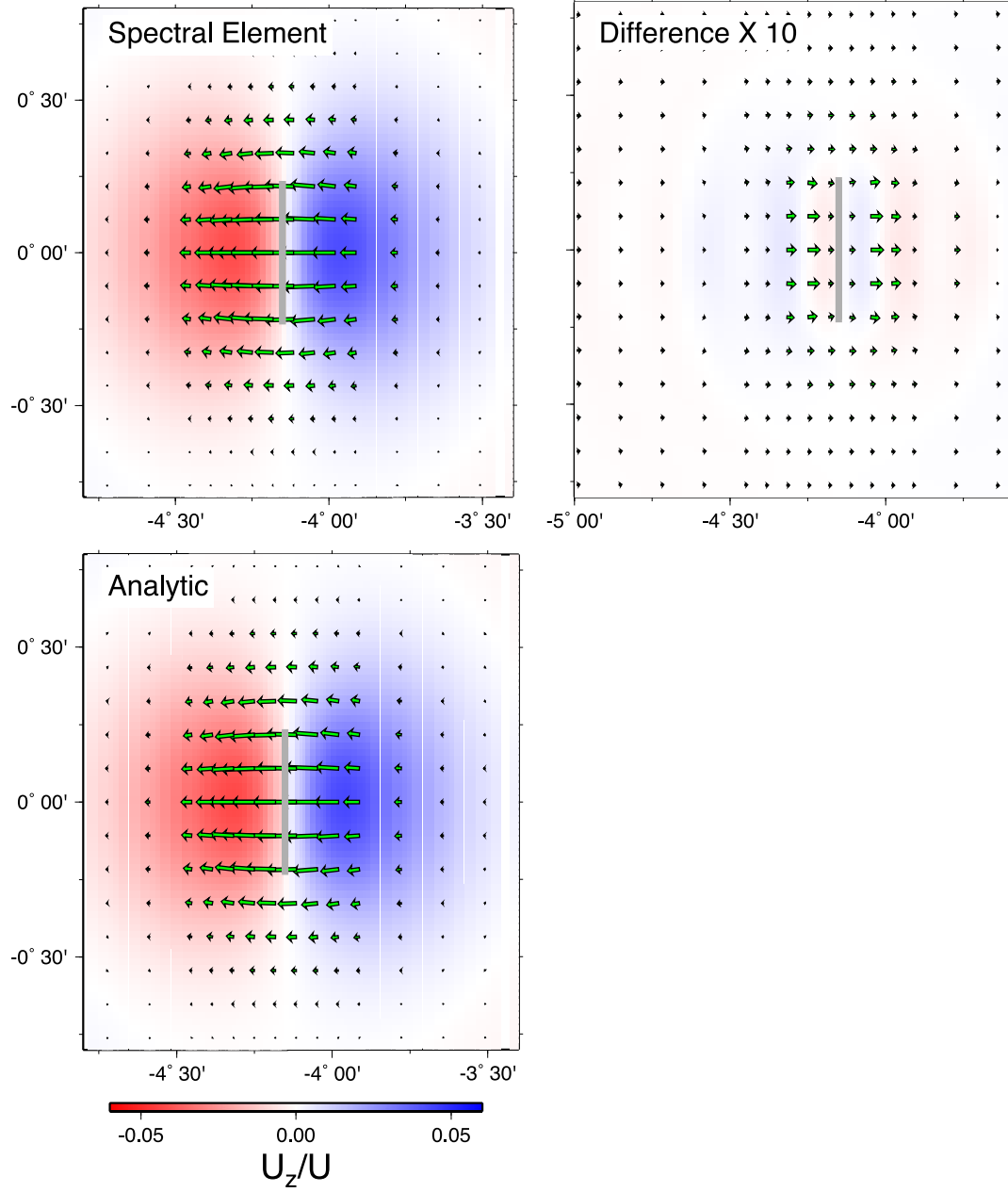


Figure 10. Close-up view of the motions following dip-slip faulting shown in Fig. 9. Right-hand plot shows difference between SEM and analytic displacement fields.

minimum wavelength of post-earthquake deformation expected at earth's surface is of the order of the elastic plate thickness (Pollitz 1997). Since the relaxation is a diffusion process, the spatial spectrum of deformation becomes longer wavelength at greater distance from the source. The minimum wavelength is about 30 km near the source and $\gg 100$ km at great distance from the source. We choose the dimension of each GLL element to be a fraction of the minimum wavelength at a given distance from the source. We choose a lateral spacing of 7.5 km near the source and 50 km near the lateral edges and a vertical spacing between 2.5 km within the elastic layer and 30 km at 180 km depth. We take 6 quadrature points per element ($N = 5$ as defined in Appendix A). This is sufficient to synthesize post-earthquake relaxation at earth's surface and within the upper half of the elastic layer, but the element sizes would need to be

reevaluated to synthesize deformation near the base of the elastic layer.

A finite seismic source is placed approximately in the middle of the model domain. We shall use both dipping thrust and vertical strike-slip sources in the examples. A stringent test of the SEM is to place the lower edge of the fault close to the top of the viscoelastic layer, where very short wavelength deformation is generated. [The minimum wavelength of deformation expected at earth's surface, however, is of the order of the elastic plate thickness (Pollitz 1997).] We choose upper and lower edge depths of the finite fault to be at 15 and 29 km, respectively, a fault length of $L = 50$ or 100 km, fault dip $\delta = 60^\circ$ or 90° and strike $\epsilon = 0$ or 45° . The fault is placed such that the great circle $\phi = 0$ bisects the fault. A finite source is realized by dividing the rectangular fault plane into a number of equal-area

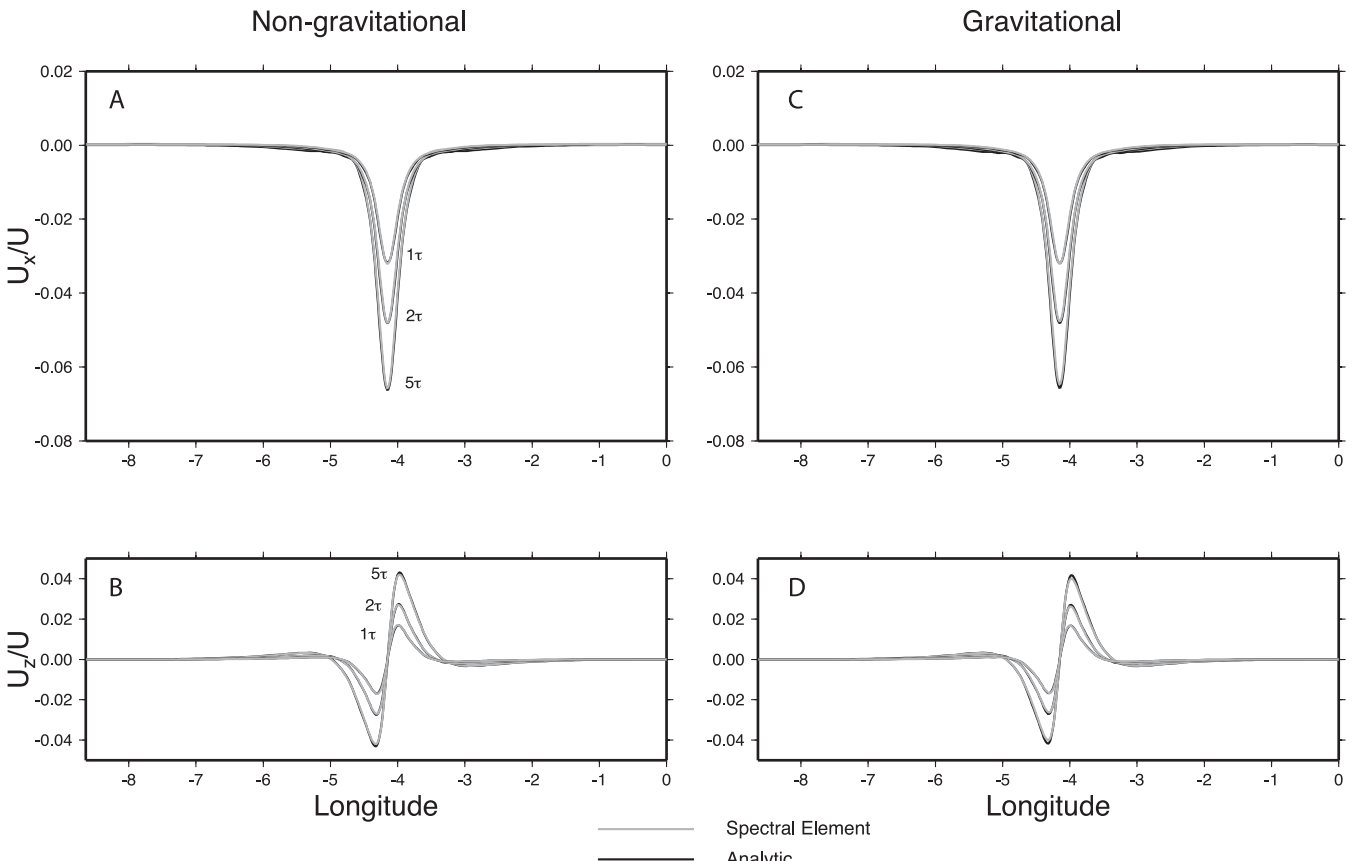


Figure 11. Ratio of horizontal displacement U_x (a, c) and vertical displacement U_z (b, d) to fault slip U for displacements following strike-slip faulting at times 1τ , 2τ and 5τ along the equator of the area shown in Fig. 9. Non-gravitational displacements from the spectral element and analytic methods are compared in (a, b), and gravitational displacements in (c, d).

patches and summing over the contribution of each point source. This is accomplished by calculating the appropriate source terms \mathbf{F} for each cell that contains one of the running point sources using eq. (B6), a step that need be done only once for each discrete Laplace transform parameter s_n and azimuthal order number m , so that the computational effort is essentially the same as that of implementing a single point source.

We assume that the source repeats in the locally north (i.e. varying ϕ) direction at intervals of $2\pi/33$ (i.e. $M = 33$ as employed in Appendix B), corresponding to approximately 1200 km (with earth radius of 6371 km), and a minimum wavelength of 30 km, so that the maximum azimuthal order number used is $m_{\max} = 1333$. The repeatability assumption leads to a reduction in computation time of a factor of 33 relative to a complete computation with $M = 1$, but this comes at a cost because it renders the solution periodic in ϕ .

In the SEM, we impose zero displacements at the lower boundary of the model domain (i.e. at $r = r_1$) and Robin boundary conditions at the lateral edges $\theta = \theta_1$ and $\theta_{N_\theta+1}$ designed to mimic the far-field displacement field. For a 3-D full space or half-space, the far-field displacements decay with distance from the source x as x^{-2} (eq. 4.34 of Aki & Richards 1980); for a medium that is bounded in one of the dimensions, for example, in the r -direction, the far-field displacements decay as x^{-1} . The latter situation is applicable to the quasi-static displacement problem, where the base of a typically thin upper elastic layer limits the domain in the r -dimension. If the lateral edges in the θ -dimension are placed a nominal distance further from the source than the total model dimension in r ($= r_{N_r+1} - r_1$), then the vertical dimension is effectively bounded at both short and long

relaxation times. This boundary condition is implemented as

$$\partial_\theta \mathbf{u}(r, \theta, \phi; s_n)|_{\theta=\theta_1} = -\frac{1}{\theta_1 - \theta_{\text{source}}} \mathbf{u}(r, \theta_1, \phi; s_n),$$

$$\partial_\theta \mathbf{u}(r, \theta, \phi; s_n)|_{\theta=\theta_{N_\theta+1}} = -\frac{1}{\theta_{N_\theta+1} - \theta_{\text{source}}} \mathbf{u}(r, \theta_{N_\theta+1}, \phi; s_n), \quad (28)$$

where θ_{source} is the θ coordinate of either a seismic point source or a representative point on a finite rupture plane. These equations are consistent with $\partial_x \mathbf{u} \sim -(1/x)\mathbf{u}$ by dividing eq. (28) by r and equating the spatial coordinate x with $r\theta$.

There are a total 171 GLL quadrature points in θ and 116 points in r . For each Laplace transform sample point, with the given reduction in summation over azimuthal order number and minimum wavelength, we require the lower-upper decomposition of 41 sparse matrices, each associated with 59 508 unknowns for a 2-D problem. The computation time for the complete 2.5-D quasi-static deformation field for a given source model is 55 CPU minutes using the linear algebra package UMFPACK (Davis 2004a,b). This defines the time-dependent deformation out to several hundred years ($\approx 150/s_{\max}$) over a volume of dimensions $\sim 900 \text{ km} \times 600 \text{ km}$ (in surface area) $\times 180 \text{ km}$ radially.

4.2 Non-gravitational case

The non-gravitational case is implemented by setting the gravitational acceleration $g_0 = 0$. The first example imposes pure dip-slip motion on a thrust fault with $\delta = 60^\circ$. The fault length is $L = 100 \text{ km}$

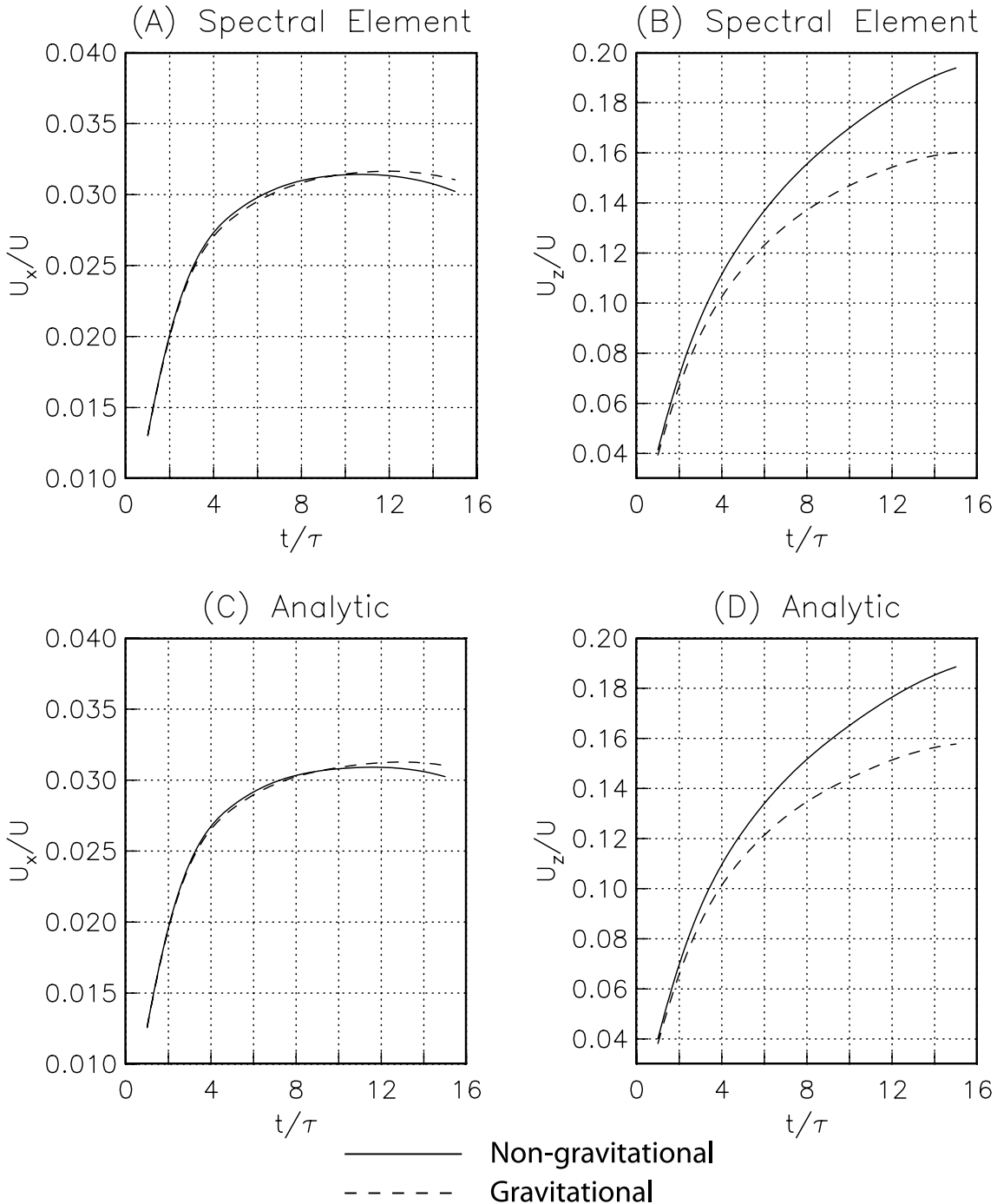


Figure 12. Time-dependent horizontal and vertical displacements, normalized by fault slip U , on the profile along the equator for the 60° -dipping thrust case for the non-gravitational and gravitational cases. (a) and (b) are SEM results, (c) and (d) are analytic results. Time is normalized by the material relaxation time τ .

and fault strike $\epsilon = 0$, that is, parallel to the θ boundaries. Defining $\tau = 2\mu/\eta$ as the material relaxation time of the ductile substrate, in Figs 3, 4 and 5(a) and (b) we compare the SEM solution of eq. (25) for cumulative post-earthquake displacements up to time $t = 5\tau$ at earth's surface with the analytic solution based on viscoelastic normal modes (Pollitz 1997); in the latter solution we employ a zero-displacement boundary condition at 180 km depth, identical to the lower boundary condition in our SEM implementation. The 3-D displacements produced by the two methods agree well

except near the θ edges of the model. The comparisons in Fig. 5 are on a profile along the equator. The curves in Fig. 5 show the cumulative displacement up to times 1τ , 2τ and 5τ . Comparison of these curves between the SEM and the analytic solution show that the time-dependent displacement is also simulated accurately. Small differences between the SEM and analytic solutions arise in part from the truncations in azimuthal order number in the SEM and spherical harmonic degree in the viscoelastic normal mode solution.

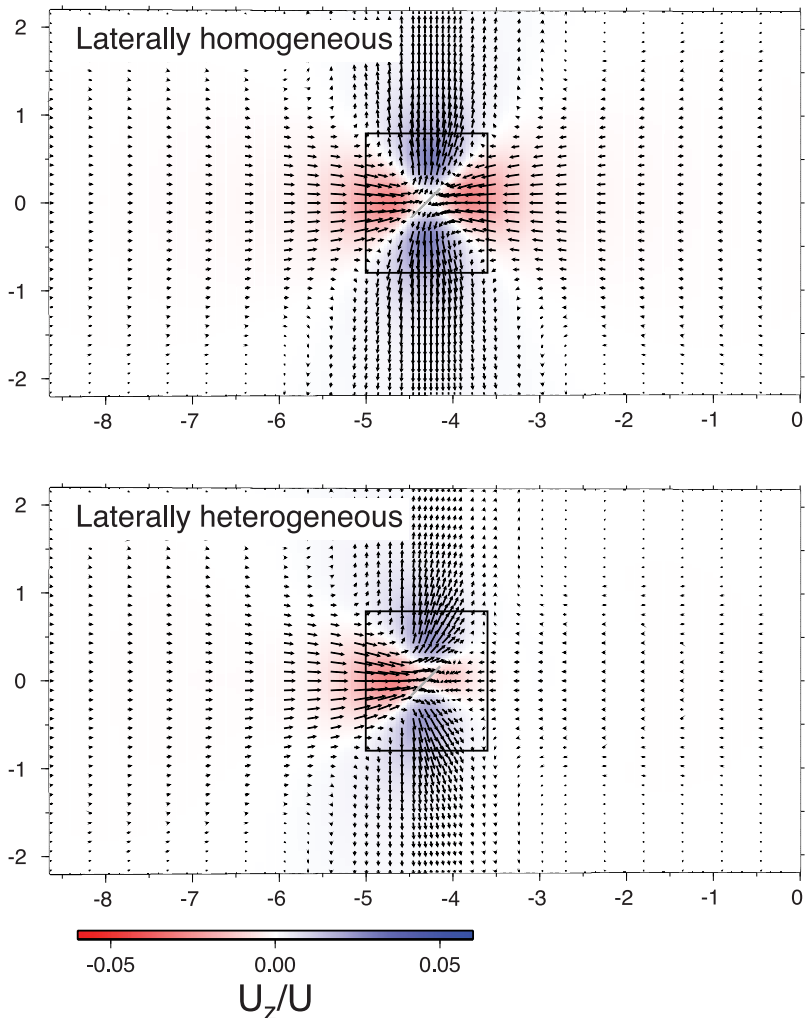


Figure 13. Horizontal displacements (arrows) and vertical displacements (colour shading) for viscoelastic-gravitational relaxation following strike-slip faulting on the fault plane indicated with the white rectangle. These are cumulative displacements up to 5τ yr following the slip event, where τ is the material relaxation time of the ductile substrate. The colour scale indicates the ratio of vertical displacement U_z to fault slip U . The two plots compare the displacement fields on the laterally homogeneous and heterogeneous models (Fig. 2). Black rectangle indicates the area plotted in Fig. 14.

Two additional examples are provided in Figs 6, 7 and 8(a) and (b) for left-lateral motion on a strike-slip fault with $L = 50$ km, $\delta = 90^\circ$, $\epsilon = 45^\circ$ and Figs 9, 10 and 11(a) and (b) for pure dip-slip motion on a vertical fault with $L = 50$ km, $\delta = 90^\circ$, $\epsilon = 0^\circ$. The 3-D displacements produced by the two methods again agree well, especially in the middle of the domain, as do the time-dependent displacements (Figs 8 and 11).

4.3 Gravitational case

The gravitational case is implemented in this example by setting $g_0 = 9.8 \text{ m s}^{-2}$ throughout the model domain, that is, ignoring radial variations in $g_0(r)$ with r . The spectral element and analytic method results times 1τ , 2τ and 5τ are compared for the various sources on the profile along the equator in Figs 5(c and d), 8(c and d), and 11(c and d). For the 60° -dipping thrust case, time-dependent displacements at the locations of maximal horizontal displacement (at longitude -4.16°) and vertical displacement (at longitude -4.04°) are compared in Fig. 12. Gravitational displacements tend to diverge from non-gravitational displacements at about $t = 3\tau$, in agreement

with results obtained by Rundle (1982) for relatively deep sources (e.g. Rundle's fig. 9).

5 LATERALLY HETEROGENEOUS CASE

We explore the post-earthquake relaxation on the laterally heterogeneous model depicted in Fig. 2(b). This structure differs from the laterally homogeneous structure used in the previous section by an increased elastic layer thickness of 100 km east of -4.15°E . For the strike-slip faulting source and gravitational case, Figs 13–15 compare horizontal and vertical displacements on the laterally heterogeneous and homogeneous models. The effect of the increased elastic thickness is clearly seen in the attenuated displacements east of -4.15°E versus those west of -4.15°E . It is notable that the displacements west of -4.15°E are of greater amplitude than those on the laterally homogeneous model, so that the side of the fault with the lower elastic layer thickness can undergo amplified deformation due to the presence of a thicker non-relaxing layer on the other side of the fault.

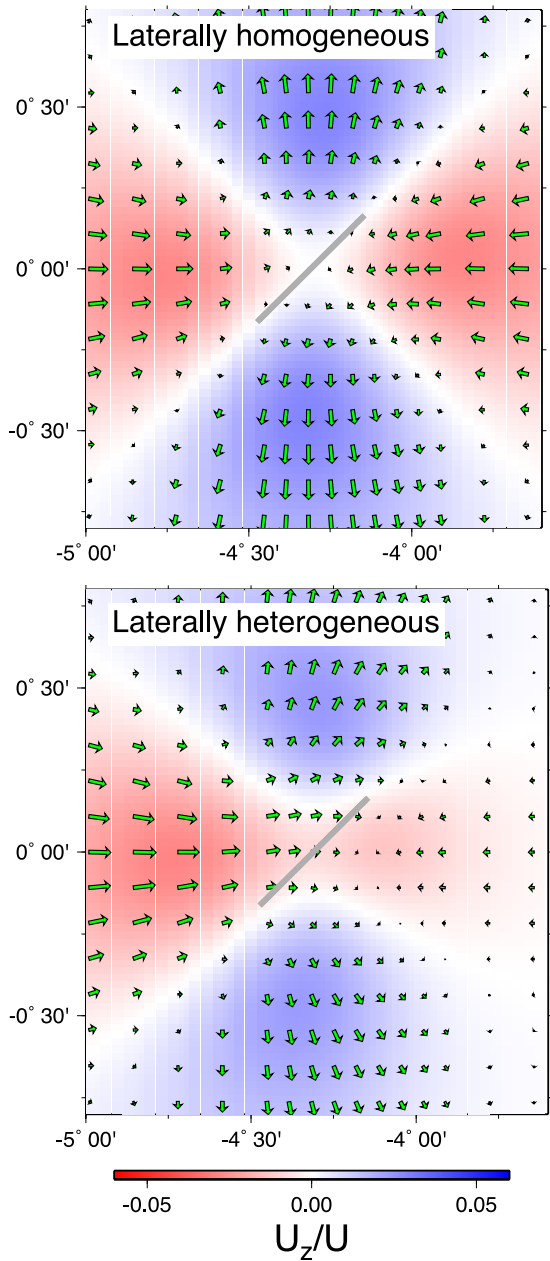


Figure 14. Close-up view of the motions following strike-slip faulting shown in Fig. 13.

6 CONCLUSIONS

The present application of the SEM to the quasi-static deformation problem is limited to the 2.5-D case, that is, 3-D deformation from a point source or finite sources implemented on axisymmetric viscoelastic structures. This renders it useful for applications where the prevailing structure varies laterally in one horizontal dimension, such as a contrast in structure across a long strike-slip fault or the presence of a dipping slab along a subduction zone that maintains constant strike in the region of interest. Although this is a limitation on eligible viscoelastic structures, the method has the advantage of speed, as the solution is essentially the sum of a series of solutions on 2-D models, which demands the inverse of relatively small stiffness matrices compared with the 3-D case.

The method relies on the correspondence principle in order to implement viscoelasticity and is, therefore, limited to linear rheolo-

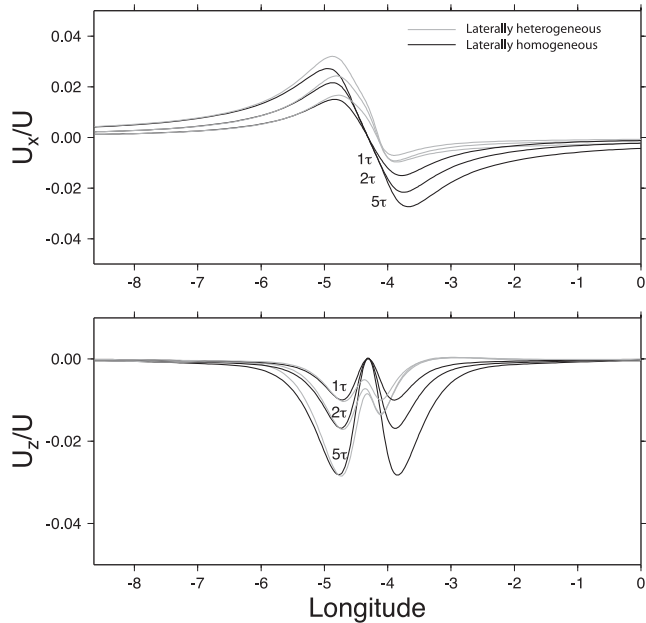


Figure 15. Ratio of horizontal displacement U_x (a) and vertical displacement U_z (b) to fault slip U for displacements following strike-slip faulting at times 1τ , 2τ and 5τ along the equator of the area shown in Fig. 13. Viscoelastic-gravitational displacements on the laterally homogeneous and laterally heterogeneous models are compared in both plots.

gies. The Maxwell rheology used in the examples can be readily replaced with more sophisticated rheologies, for example, a Burgers body (Pollitz 2003a), generalized Burgers body (Ivins 1996) or a combined Maxwell and absorption band model (Yuen & Peltier 1982).

ACKNOWLEDGEMENTS

I thank Christina Morency and Brad Aagaard for their reviews of a preliminary draft and Andrew Bradley for assistance with implementing the linear algebra package used in this study. This paper benefitted from the constructive criticisms of Dr. David Al-Attar, an anonymous reviewer, and the Associate Editor.

REFERENCES

- Aagaard, B., Knepley, M. & Williams, C., 2013. A domain decomposition approach to implementing fault slip in finite-element models of quasi-static and dynamic crustal deformation, *J. geophys. Res.*, **118**, doi:10.1002/jgrb.50217.
- Aki, K. & Richards, P.G., 1980. *Quantitative Seismology*, Vol. 1, W.H. Freeman and Company.
- Al-Attar, D. & Tromp, J., 2014. Sensitivity kernels for viscoelastic loading based on adjoint methods, *Geophys. J. Int.*, **196**(1), 34–77.
- Barbot, S. & Fialko, Y., 2010a. Fourier-domain green function for an elastic semi-infinite solid under gravity, with applications to earthquake and volcano deformation, *Geophys. J. Int.*, **182**, 568–582.
- Barbot, S. & Fialko, Y., 2010b. A unified continuum representation of post-seismic relaxation mechanisms: semi-analytic models of afterslip, poroelastic rebound and viscoelastic flow, *Geophys. J. Int.*, **182**, 1124–1140.
- Bills, B.G., Currey, D.R. & Marshall, G.A., 1994. Viscosity estimates for the crust and upper mantle from patterns of lacustrine shoreline deformation in the Eastern Great Basin, *J. geophys. Res.*, **99**(B11), 22 059–22 086.
- Bland, D., 1960. *The Theory of Linear Viscoelasticity*, Pergamon Press.

- Brothers, D., Kilb, D., Luttrell, K., Driscoll, N. & Kent, G., 2011. Loading of the San Andreas fault by flood-induced rupture of faults beneath the Salton Sea, *Nat. Geosci.*, **35**, doi:10.1038/NGEO1184.
- Bürgmann, R. & Dresen, G., 2008. Rheology of the lower crust and upper mantle: evidence from rock mechanics, geodesy, and field observations, *Ann. Rev. Earth planet. Sci.*, **36**, 531–567.
- Canuto, C., Hussaini, M.Y., Quarteroni, A. & Zang, T.A., 1988. *Spectral Methods in Fluid Dynamics*, Springer-Verlag.
- Dahlen, F.A. & Tromp, J., 1998. *Theoretical Global Seismology*, Princeton University Press.
- Davis, T., 2004a. A column pre-ordering strategy for the unsymmetric-pattern multifrontal method, *ACM Trans. Math. Software*, **30**, 165–195.
- Davis, T., 2004b. Algorithm 832: UMFPACK, an unsymmetric-pattern multifrontal method, *ACM Trans. Math. Software*, **30**, 196–199.
- Fernandez, J. & Rundle, J.B., 2004. Postseismic viscoelastic-gravitational half space computations: problems and solutions, *Geophys. Res. Lett.*, **31**, doi:10.1029/2004GL019654.
- Fichtner, A., 2011. *Full Seismic Waveform Modelling and Inversion*, Springer-Verlag.
- Freed, A.M. & Bürgmann, R., 2004. Evidence of powerlaw flow in the Mojave Desert mantle, *Nature*, **430**, 548–551.
- Freed, A.M., Bürgmann, R. & Herring, T., 2007. Far-reaching transient motions after Mojave earthquakes require broad mantle flow beneath a strong crust, *Geophys. Res. Lett.*, **34**, L06312, doi:10.1029/2006GL029155.
- Hammond, W.C., Kreemer, C. & Blewitt, G., 2009. Geodetic constraints on contemporary deformation in the northern Walker Lane: 3. Central Nevada Seismic Belt postseismic relaxation, in *Late Cenozoic Structure and Evolution of the Great Basin Sierra Nevada Transition*, Special Paper 447, pp. 33–54, eds Oldow, J.S. & Cashman, P.H., Geological Society of America.
- Hearn, E.H., McClusky, S., Ergintav, S. & Reilinger, R.E., 2009. Izmit earthquake postseismic deformation and dynamics of the North Anatolian Fault Zone, *J. geophys. Res.*, **114**, B08405, doi:10.1029/2008JB006026.
- Hu, Y. & Wang, K., 2012. Spherical-Earth finite element model of short-term postseismic deformation following the 2004 Sumatra earthquake, *J. geophys. Res.*, **117**, B05404, doi:10.1029/2012JB009153.
- Ivins, E.R., 1996. Transient creep of a composite lower crust, 2, a polymineralic basis for rapidly evolving postseismic deformation modes, *J. geophys. Res.*, **101**, 28 005–28 028.
- Karniadakis, G.E. & Sherwin, S.J., 1999. *Spectral/hp Element Method for CFD*, Oxford University Press.
- Kaufmann, G. & Amelung, F., 2000. Reservoir-induced deformation and continental rheology in the vicinity of Lake Mead, Nevada, *J. geophys. Res.*, **105**, 16 341–16 358.
- Komatitsch, D. & Tromp, J., 1999. Introduction to the spectral element method for three-dimensional seismic wave propagation, *Geophys. J. Int.*, **139**, 806–822.
- Komatitsch, D. & Tromp, J., 2002a. Spectral element simulations of global seismic wave propagation—I. Validation, *Geophys. J. Int.*, **149**, 390–412.
- Komatitsch, D. & Tromp, J., 2002b. Spectral element simulations of global seismic wave propagation—II. Three-dimensional models, oceans, rotation, and self-gravitation, *Geophys. J. Int.*, **150**, 303–318.
- Komatitsch, D. & Vilotte, J., 1998. The spectral-element method: an efficient tool to simulate the seismic response of 2D and 3D geological structures, *Bull. seism. Soc. Am.*, **88**, 368–392.
- Luttrell, K., Sandwell, D., Smith-Konter, B., Bills, B. & Bock, Y., 2007. Modulation of the earthquake cycle at the southern San Andreas fault by lake loading, *J. geophys. Res.*, **112**, B08411, doi:10.1029/2006JB004752.
- Malservisi, R., Furlong, K.P. & Dixon, T.H., 2001. Influence of the earthquake cycle and lithospheric rheology on the dynamics of the Eastern California Shear Zone, *Geophys. Res. Lett.*, **28**, 2731–2734.
- Melosh, H.J. & Raefsky, A., 1980. The dynamical origin of subduction zone topography, *Geophys. J. R. astr. Soc.*, **60**, 333–354.
- Nissen-Meyer, T., Fournier, A. & Dahlen, F.A., 2007. A two-dimensional spectral-element method for computing spherical-earth seismograms I. Moment-tensor source, *J. geophys. Res.*, **168**(3), 1067–1092.
- Parker, J., Lyzenga, G., Norton, C., Zuffada, C., Glasscoe, M., Lou, J. & Donnellan, A., 2008. Geophysical Finite-Element Simulation Tool (GeoFEST): algorithms and validation for quasistatic regional faulted crust problems, in *Earthquakes: Simulations, Sources and Tsunamis*, pp. 497–521, eds Tiampo, K.F., Weatherley, D.K. & Weinstein, S.A., Birkhäuser Verlag.
- Piersanti, A., Spada, G., Sabadini, R. & Bonafede, M., 1995. Global post-seismic deformation, *Geophys. J. Int.*, **120**, 544–566.
- Pollitz, F., Banerjee, P., Grjalva, K., Nagarajan, B. & Bürgmann, R., 2008. Effect of 3D viscoelastic structure on postseismic relaxation from the M=9.2 Sumatra earthquake, *Geophys. J. Int.*, **172**, 189–204.
- Pollitz, F., Bürgmann, R. & Thatcher, W., 2012. Illumination rheological mantle heterogeneity by the M7.2 2010 El Mayor-Cucapah earthquake, *Geochem. Geophys. Geosyst.*, **13**, Q06002, doi:10.1029/2012GC004139.
- Pollitz, F.F., 1997. Gravitational viscoelastic postseismic relaxation on a layered spherical earth, *J. geophys. Res.*, **102**, 17 921–17 941.
- Pollitz, F.F., 2003a. Transient rheology of the uppermost mantle beneath the Mojave Desert, California, *Earth planet. Sci. Lett.*, **215**, 89–104.
- Pollitz, F.F., 2003b. Postseismic relaxation theory on a laterally heterogeneous viscoelastic model, *Geophys. J. Int.*, **155**, 57–78.
- Pollitz, F.F., Banerjee, P. & Bürgmann, R., 2006. Postseismic relaxation following the great 2004 Sumatra-Andaman earthquake on a compressible self-gravitating Earth, *Geophys. J. Int.*, **167**, 397–420.
- Rundle, J.B., 1980. Static elastic-gravitational deformation of a layered half space by point couple sources, *J. geophys. Res.*, **85**, 5354–6363.
- Rundle, J.B., 1981. Vertical displacements from a rectangular fault in a layered elastic-gravitational media, *J. Phys. Earth*, **29**, 173–186.
- Rundle, J.B., 1982. Viscoelastic-gravitational deformation by a rectangular thrust fault in a layered Earth, *J. geophys. Res.*, **87**, 7787–7796.
- Ryder, I., Bürgmann, R. & Pollitz, F.F., 2011. Lower crustal relaxation beneath the Tibetan Plateau and Qaidam Basin following the 2001 Kokoxili earthquake, *Geophys. J. Int.*, **197**, doi:10.1111/j.1365-1246.X.2011.05179.x.
- Segall, P., 2010. *Earthquake and Volcano Deformation*, Princeton University Press.
- Thatcher, W. & Pollitz, F.F., 2008. Temporal evolution of continental lithospheric strength in actively deforming regions, *GSA Today*, **18**, 4–11.
- Wang, R., Lorenzo-Martin, F. & Roth, F., 2006. PSGRN/PSCMP—a new code for calculating co- and post-seismic deformation, geoid and gravity changes based on the viscoelastic-gravitational dislocation theory, *Comput. Geosci.*, **32**, 527–541.
- Yuen, D.A. & Peltier, W.R., 1982. Normal modes of the viscoelastic earth, *Geophys. J. R. astr. Soc.*, **69**, 495–526.
- Zeng, Y., 2001. Viscoelastic stress-triggering of the 1999 Hector Mine earthquake by the 1992 Landers earthquake, *Geophys. Res. Lett.*, **28**, 3007–3010.
- Zhong, S., Paulson, A. & Wahr, J., 2003. Three-dimensional finite-element modelling of Earth's viscoelastic deformation: effects of lateral variations in lithospheric thickness, *Geophys. J. Int.*, **155**, 679–695.

APPENDIX A: PROPERTIES OF GAUSS-LEGENDRE-LOBATTO FUNCTIONS

Details of the mathematical background of GLL quadrature are presented in various works (e.g. Canuto *et al.* 1988; Karniadakis & Sherwin 1999; Fichtner 2011). Here are summarized a few of the relevant properties.

1-D GLL basis functions ψ_γ are defined as Lagrange interpolation polynomials using GLL quadrature points. They are given by

$$\psi_\gamma(x) = \frac{-1}{N(N+1)P_N(x_\gamma)} \frac{(1-x^2)P'_N(x)}{x - x_\gamma}, \quad (\text{A1})$$

where $P_N(x)$ is the Legendre polynomial of order N . The quadrature points $\{x_\gamma\}$ are the $N - 1$ zeroes of $P'_N(x)$ augmented by -1 and $+1$. The $\{\psi_\gamma\}$ form a mutually orthogonal basis set and have the property

$$\psi_\gamma(x_\nu) = \delta_{\gamma\nu}, \quad \gamma, \nu = 0, \dots, N. \quad (\text{A2})$$

Using Legendre's equation

$$(1 - x^2) P''(x) - 2x P'_N(x) + N(N + 1)P_N(x) = 0, \quad (\text{A3})$$

the x-derivative of $\psi_\gamma(x)$ is

$$\psi'_\gamma(x) = \frac{-\psi_\gamma(x) + P_N(x)/P_N(x_\gamma)}{x - x_\gamma}. \quad (\text{A4})$$

From eqs (A2) and (A4), the derivative at the 1-D quadrature points is

$$\psi'_\gamma(x_\nu) = \frac{1}{P_N(x_\gamma)} \frac{P_N(x_\nu)}{x_\nu - x_\gamma} \quad (\nu \neq \gamma). \quad (\text{A5})$$

Applying L'Hospital's rule to eq. (A4) near $x = x_\gamma$ yields

$$\psi'_\gamma(x_\gamma) = \frac{1}{2} \frac{P'_N(x_\gamma)}{P_N(x_\gamma)}. \quad (\text{A6})$$

2-D GLL basis functions are denoted

$$\psi_{\alpha\beta}(x, z) = \psi_\alpha(x) \psi_\beta(z). \quad (\text{A7})$$

The $\{\psi_{\alpha\beta}\}$ form a mutually orthogonal basis set in 2-D. At the 2-D quadrature points,

$$\psi_{\alpha\beta}(x_\gamma, x_\nu) = \delta_{\alpha\gamma} \delta_{\beta\nu}, \quad (\text{A8})$$

$$\partial_x \psi_{\alpha\beta}(x, z)|_{x=x_\gamma, z=x_\nu} = \psi'_\alpha(x)|_{x=x_\gamma} \psi_\beta(x_\nu), \quad (\text{A9})$$

$$\partial_z \psi_{\alpha\beta}(x, z)|_{x=x_\gamma, z=x_\nu} = \psi_\beta(x_\gamma) \psi'_\beta(z)|_{z=x_\nu}. \quad (\text{A10})$$

The 1-D Lagrangian interpolant is

$$f(x) \approx \sum_\gamma f(x_\gamma) \psi_\gamma(x). \quad (\text{A11})$$

The 1-D Gauss–Lobatto quadrature rule takes the form

$$\int_{-1}^1 f(x) dx \approx \sum_\gamma w_\gamma f(x_\gamma), \quad (\text{A12})$$

where the weights are given by

$$w_\gamma = \frac{2}{N(N+1)} \frac{1}{[P_N(x_\gamma)]^2} \quad (\gamma = 0, \dots, N). \quad (\text{A13})$$

The interpolant eq. (A11) exhibits spectral convergence with increasing N , for example, for an analytic function the error in the approximation diminishes faster than any inverse power of N (Canuto *et al.* 1988), and eq. (A12) is exact for polynomial functions up to degree $2N - 1$. The 2-D Gauss–Lobatto quadrature rule is

$$\int_{-1}^1 \int_{-1}^1 f(x, z) dx dz \approx \sum_\gamma \sum_\nu w_\gamma w_\nu f(x_\gamma, x_\nu). \quad (\text{A14})$$

APPENDIX B: SOURCE TERM

We implement a seismic point source of the form

$$\mathbf{f}(\mathbf{r}; s) = -\mathbf{M} \cdot \nabla \delta(\mathbf{r} - \mathbf{r}_0) \frac{1}{s}, \quad (\text{B1})$$

where \mathbf{M} is the moment tensor, \mathbf{r}_0 is the location of the point source and $\delta(\mathbf{r} - \mathbf{r}_0)$ is the Dirac delta function. The source location is $\mathbf{r}_0 = (r_0, \theta_0, \phi_0)$. We have assumed a $H(t)$ time dependence for \mathbf{f} , where $H(t)$ is the Heaviside step function. We also assume that this force is periodic in azimuth with M sources evenly spaced in ϕ at constant $r = r_0$ and $\theta = \theta_0$.

Let the point source be located within element Γ . In eq. (12) we choose a scalar function of the form

$$w(r, \theta) = \psi_p(x(r, \theta), z(r, \theta)), \quad (\text{B2})$$

where ψ_p is a 2-D GLL basis function defined in Appendix A, $p = 1, \dots, (N + 1)^2$. With a test function $\mathbf{w}(\mathbf{r})$ of the form of eq. (12), we then evaluate the integral of the source term of eq. (13), that is,

$$\mathbf{F} = \frac{1}{2\pi} \int_0^{2\pi} \int_{\Gamma} \psi_p(x(r, \theta), z(r, \theta)) e^{-im\phi} \begin{pmatrix} \hat{\theta} \\ \hat{\phi} \\ \hat{\mathbf{r}} \end{pmatrix} \cdot \mathbf{M} \cdot \nabla \delta(\mathbf{r} - \mathbf{r}_0) \frac{1}{s} r \sin \theta d^2 \mathbf{r} d\phi \quad (\text{B3})$$

The Dirac delta function may be written in spherical coordinates as

$$\delta(\mathbf{r} - \mathbf{r}_0) = \frac{1}{r^2 \sin \theta} \delta(\theta - \theta_0) \delta(\phi - \phi_0) \delta(r - r_0). \quad (\text{B4})$$

With integration by parts with respect to ϕ this leads to

$$\int_0^{2\pi} e^{-im\phi} \begin{pmatrix} \hat{\theta} \\ \hat{\phi} \\ \hat{\mathbf{r}} \end{pmatrix} \cdot \mathbf{M} \cdot \nabla \delta(\mathbf{r} - \mathbf{r}_0) \frac{1}{s} d\phi = \frac{M}{r^2 \sin \theta} \frac{1}{s} e^{-im\phi_0} \times \begin{pmatrix} M_{\theta\theta} \frac{1}{r} \partial_\theta \delta(\theta - \theta_0) \delta(r - r_0) + \frac{im}{r \sin \theta} M_{\theta\phi} \delta(\theta - \theta_0) \delta(r - r_0) + M_{r\theta} \delta(\theta - \theta_0) \partial_r \delta(r - r_0) \\ M_{\theta\phi} \frac{1}{r} \partial_\theta \delta(\theta - \theta_0) \delta(r - r_0) + \frac{im}{r \sin \theta} M_{\phi\phi} \delta(\theta - \theta_0) \delta(r - r_0) + M_{r\phi} \delta(\theta - \theta_0) \partial_r \delta(r - r_0) \\ M_{r\theta} \frac{1}{r} \partial_\theta \delta(\theta - \theta_0) \delta(r - r_0) + \frac{im}{r \sin \theta} M_{r\phi} \delta(\theta - \theta_0) \delta(r - r_0) + M_{rr} \delta(\theta - \theta_0) \partial_r \delta(r - r_0) \end{pmatrix}. \quad (\text{B5})$$

Substituting eq. (B5) into eq. (B3), using the relation $d^2 \mathbf{r} = r dr d\theta$, integrating by parts with respect to θ or r and using eq. (19) yields

$$\mathbf{F} = \frac{1}{2\pi} M \frac{1}{s} e^{-im\phi_0} \times \begin{pmatrix} -M_{\theta\theta} \frac{1}{r_0} \partial_x \psi_p(x, z)|_{x_0, z_0} \left(\frac{\Delta\theta^\Gamma}{2} \right)^{-1} + \frac{im}{r \sin \theta} M_{\theta\phi} \psi_p(x_0, z_0) - M_{r\theta} \partial_z \psi_p(x, z)|_{x_0, z_0} \left(\frac{\Delta r^\Gamma}{2} \right)^{-1} \\ -M_{\theta\phi} \frac{1}{r_0} \partial_x \psi_p(x, z)|_{x_0, z_0} \left(\frac{\Delta\theta^\Gamma}{2} \right)^{-1} + \frac{im}{r \sin \theta} M_{\phi\phi} \psi_p(x_0, z_0) - M_{r\phi} \partial_z \psi_p(x, z)|_{x_0, z_0} \left(\frac{\Delta r^\Gamma}{2} \right)^{-1} \\ -M_{r\theta} \frac{1}{r_0} \partial_x \psi_p(x, z)|_{x_0, z_0} \left(\frac{\Delta\theta^\Gamma}{2} \right)^{-1} + \frac{im}{r \sin \theta} M_{r\phi} \psi_p(x_0, z_0) - M_{rr} \partial_z \psi_p(x, z)|_{x_0, z_0} \left(\frac{\Delta r^\Gamma}{2} \right)^{-1} \end{pmatrix}, \quad (\text{B6})$$

where $(x_0, z_0) = (x(r_0, \theta_0), y(r_0, \theta_0))$. Note that because of the assumed distribution of sources, \mathbf{F} is non-zero only for m equal to an integer multiple of M .

APPENDIX C: STIFFNESS MATRIX

For element Γ we evaluate the left-hand-side of eq. (14) as the product of a stiffness matrix \mathbf{K} and a model vector \mathbf{U} containing the unknown displacement coefficients at the nodes. In eq. (12) we choose the scalar function $w(r, \theta)$ given by eq. (B2). We write out the left-hand side of eq. (14) by substituting the test function $\mathbf{w}(r, \theta)$ of eq. (12), expanding the 3-D integration element $d^3 \mathbf{r} = r^2 \sin \theta dr d\theta d\phi$, and making use of the gradient in spherical coordinates

$$\nabla = \frac{\partial}{\partial r} \hat{\mathbf{r}} + \frac{1}{r} \frac{\partial}{\partial \theta} \hat{\theta} + \frac{1}{r \sin \theta} \frac{\partial}{\partial \phi} \hat{\phi}, \quad (\text{C1})$$

and the relations

$$\begin{aligned} \partial_r \hat{\mathbf{r}} &= \mathbf{0}, & \partial_r \hat{\theta} &= \mathbf{0}, & \partial_r \hat{\phi} &= \mathbf{0} \\ \partial_\theta \hat{\mathbf{r}} &= \hat{\theta}, & \partial_\theta \hat{\theta} &= -\hat{\mathbf{r}}, & \partial_\theta \hat{\phi} &= \mathbf{0} \\ \partial_\phi \hat{\mathbf{r}} &= \sin \theta \hat{\phi}, & \partial_\phi \hat{\theta} &= \cos \theta \hat{\phi}, & \partial_\phi \hat{\phi} &= -\sin \theta \hat{\mathbf{r}} - \cos \theta \hat{\theta}. \end{aligned} \quad (\text{C2})$$

This yields three expressions, one for each component of \mathbf{w} , which we write in the form

$$\frac{1}{2\pi} \int_0^{2\pi} d\phi \int_{\Gamma} dr d\theta r^2 \sin \theta \left\{ \psi_p(x(r, \theta), z(r, \theta)) e^{-im\phi} \begin{pmatrix} \hat{\theta} \\ \hat{\phi} \\ \hat{\mathbf{r}} \end{pmatrix} \right.$$

$$\rho(\mathbf{r}) \{ \nabla [\mathbf{u}(\mathbf{r}; s) \cdot \mathbf{g}] - [\nabla \cdot \mathbf{u}(\mathbf{r}; s)] \mathbf{g} \}$$

$$\left. -\nabla (\psi_p(x(r, \theta), z(r, \theta)) e^{-im\phi}) \begin{pmatrix} \hat{\theta} \\ \hat{\phi} \\ \hat{\mathbf{r}} \end{pmatrix} : \boldsymbol{\sigma}(\mathbf{r}; s) \right\}$$

$$-r^{-1}\psi_p(x(r,\theta),z(r,\theta))\begin{pmatrix} -\hat{\mathbf{r}}\hat{\theta} + \cot\theta\hat{\phi}\hat{\phi} \\ -\hat{\mathbf{r}}\hat{\phi} - \cot\theta\hat{\theta}\hat{\phi} \\ \hat{\theta}\hat{\theta} + \hat{\phi}\hat{\phi} \end{pmatrix} e^{-im\phi} : \boldsymbol{\sigma}(\mathbf{r};s) \Bigg\}. \quad (\text{C3})$$

The surface integral over ∂V in eq. (14) has been omitted in eq. (C3) by virtue of the boundary conditions, which involve vanishing ψ_p on the θ boundaries and lower r boundary and vanishing $\hat{\mathbf{n}} \cdot \boldsymbol{\sigma}$ on the upper r boundary.

For the present purpose, it is convenient to let p refer to one of the global nodes at which one or more elemental ψ_p has a value of unity. If this node is shared by more than one element, then the applicable ψ_p is a union of the non-overlapping elemental ψ_p which share that node. With integration increments $dr = \frac{\Delta r^\Gamma}{2} dz$ and $d\theta = \frac{\Delta\theta^\Gamma}{2} dx$ (eq. 19) and applying the 2-D integration rule (eq. A14) to eq. (C3) yields

$$\begin{aligned} (\mathbf{KU})_{\text{rows } 3p-2, 3p-1, 3p} &= \sum_\gamma \sum_v w_\gamma w_v r_{\gamma v}^2 \sin\theta_{\gamma v} \frac{\Delta r^\Gamma}{2} \frac{\Delta\theta^\Gamma}{2} \frac{1}{2\pi} \int_0^{2\pi} d\phi \\ &\left\{ \psi_p(x_\gamma, z_v) e^{-im\phi} \begin{pmatrix} \hat{\theta} \\ \hat{\phi} \\ \hat{\mathbf{r}} \end{pmatrix} \cdot \rho(r_{\gamma v}, \theta_{\gamma v}, \phi) \{ \nabla [\mathbf{r}(r, \theta, \phi; s) \cdot \mathbf{g}(r)] - [\nabla \cdot \mathbf{r}(r, \theta, \phi; s)] \mathbf{g}(r_{\gamma v}) \} \Big|_{\theta=\theta_{\gamma v}, r=r_{\gamma v}} \right. \\ &- \nabla (\psi_p(x(r, \theta), z(r, \theta)) e^{-im\phi}) \Big|_{\theta=\theta_{\gamma v}, r=r_{\gamma v}} \begin{pmatrix} \hat{\theta} \\ \hat{\phi} \\ \hat{\mathbf{r}} \end{pmatrix} : \boldsymbol{\sigma}(r_{\gamma v}, \theta_{\gamma v}, \phi; s) \\ &\left. - r_{\gamma v}^{-1} \psi_p(x_\gamma, z_v) \begin{pmatrix} -\hat{\mathbf{r}}\hat{\theta} + \cot\theta_{\gamma v}\hat{\theta}\hat{\phi} \\ -\hat{\mathbf{r}}\hat{\phi} - \cot\theta_{\gamma v}\hat{\theta}\hat{\phi} \\ \hat{\theta}\hat{\theta} + \hat{\phi}\hat{\phi} \end{pmatrix} e^{-im\phi} : \boldsymbol{\sigma}(r_{\gamma v}, \theta_{\gamma v}, \phi; s) \right\} \quad (\text{C4}) \end{aligned}$$

where $r_{\gamma v}$ and $\theta_{\gamma v}$ are given by eqs (17) and (18), respectively, and $\hat{\theta}$, $\hat{\phi}$ and $\hat{\mathbf{r}}$ are the unit vectors at position $(r_{\gamma v}, \theta_{\gamma v}, \phi)$. From eqs (19) and (C1), the term involving the gradient of $\psi_p(x(r, \theta), z(r, \theta)) e^{-im\phi}$ with respect to global coordinates may be expressed in terms of spatial derivatives with respect to the elemental coordinates x and z :

$$\begin{aligned} \nabla (\psi_p(x(r, \theta), z(r, \theta)) e^{-im\phi}) \Big|_{\theta=\theta_{\gamma v}, r=r_{\gamma v}} &= \left\{ \frac{\partial}{\partial z} \psi_p(x, z) \left(\frac{\Delta r^\Gamma}{2} \right)^{-1} \hat{\mathbf{r}} + \frac{1}{r_{\gamma v}} \frac{\partial}{\partial x} \psi_p(x, z) \left(\frac{\Delta\theta^\Gamma}{2} \right)^{-1} \hat{\theta} \right. \\ &\left. - \frac{im}{r_{\gamma v} \sin\theta_{\gamma v}} \psi_p(x, z) \hat{\phi} \right\} e^{-im\phi} \Big|_{x=x_\gamma, z=z_v} \quad (\text{C5}) \end{aligned}$$

Eq. (C4) is valid for an anisotropic viscoelastic medium. Let the displacement components in the $r - \theta - \phi$ coordinate system be u_r , u_θ and u_ϕ . The strain tensor at $\mathbf{r} = (r, \theta, \phi)$ is given by eq. (A.139) of Dahlen & Tromp (1998). For an isotropic medium with Lamé parameters λ and μ , the stress tensor then has components

$$\begin{aligned} \sigma_{\theta\theta} &= (\lambda + 2\mu) \frac{\partial_\theta u_\theta + u_r}{r} + \lambda \left(\partial_r u_r + \frac{\partial_\phi u_\phi}{r \sin\theta} + \frac{u_r}{r} + \frac{u_\theta \cot\theta}{r} \right), \\ \sigma_{\phi\phi} &= (\lambda + 2\mu) \left(\frac{\partial_\phi u_\phi}{r \sin\theta} + \frac{u_r}{r} + \frac{u_\theta \cot\theta}{r} \right) + \lambda \left(\frac{\partial_\theta u_\theta + u_r}{r} + \partial_r u_r \right), \\ \sigma_{rr} &= (\lambda + 2\mu) \partial_r u_r + \lambda \left(\frac{\partial_\theta u_\theta + u_r}{r} + \frac{\partial_\phi u_\phi}{r \sin\theta} + \frac{u_r}{r} + \frac{u_\theta \cot\theta}{r} \right), \\ \sigma_{\phi r} &= \mu \left(\partial_r u_\phi + \frac{\partial_\phi u_r}{r \sin\theta} - \frac{u_\phi}{r} \right), \\ \sigma_{\theta r} &= \mu \left(\partial_r u_\theta + \frac{\partial_\theta u_r}{r} - \frac{u_\theta}{r} \right), \\ \sigma_{\theta\phi} &= \mu \left(\frac{\partial_\theta u_\phi}{r} + \frac{\partial_\phi u_\theta}{r \sin\theta} - \frac{u_\phi \cot\theta}{r} \right), \quad (\text{C6}) \end{aligned}$$

where $\mu = \mu(r, \theta; s)$ and $\lambda = \lambda(r, \theta; s)$ are the appropriate s -dependent elastic moduli for a linear viscoelastic rheology.

Terms involving the stress tensor that appear in eq. (C4) may be related to the displacement expansion coefficients by substituting the displacement field of eq. (20) into eq. (C6) and evaluating the integral over ϕ . This yields, for example,

$$\frac{1}{2\pi} \int_0^{2\pi} \sigma_{\theta r}(r_{\gamma v}, \theta_{\gamma v}, \phi; s) e^{-im\phi} d\phi = \mu(r_{\gamma v}, \theta_{\gamma v}; s) \sum_{\alpha=0}^N \sum_{\beta=0}^N \left[a_{\alpha\beta}^m \frac{\partial}{\partial z} \psi_{\alpha\beta}(x, z) \left(\frac{\Delta r^\Gamma}{2} \right)^{-1} + c_{\alpha\beta}^m \frac{1}{r_{\gamma v}} \frac{\partial}{\partial x} \psi_{\alpha\beta}(x, z) \left(\frac{\Delta\theta^\Gamma}{2} \right)^{-1} - a_{\alpha\beta}^m \frac{1}{r_{\gamma v}} \psi_{\alpha\beta}(x, z) \right] \Big|_{x=x_\gamma, z=z_v} \quad (C7)$$

and similarly for other stress components as well as the gravitational terms. Substitution of eq. (C6) into eq. (C4), using eq. (C5) and the relations of stress components and gravitational terms to the $\{a_{\alpha\beta}^m, b_{\alpha\beta}^m, c_{\alpha\beta}^m\}$ (e.g. eq. C7), then yields the stiffness matrix. Note that because of the use of M repeating sources distributed evenly in ϕ (Appendix B), only those displacement coefficients associated with m equal to an integer multiple of M need be retained.

APPENDIX D: SYMMETRIES OF EXPANSION COEFFICIENTS

The computational efficiency of employing eq. (20) for the expansion coefficients $a_{\alpha\beta}^m$, $b_{\alpha\beta}^m$ and $c_{\alpha\beta}^m$ may be increased by taking advantage of symmetries with respect to azimuthal order number. Note that each expansion coefficient receives separate contributions from the $\cos(m\phi_0)$ and $\sin(m\phi_0)$ source terms of eq. (B6), that is,

$$\begin{aligned} a_{\alpha\beta}^m &= a_{\alpha\beta}^m[\cos(m\phi_0) \text{ term}] + a_{\alpha\beta}^m[\sin(m\phi_0) \text{ term}], \\ b_{\alpha\beta}^m &= b_{\alpha\beta}^m[\cos(m\phi_0) \text{ term}] + b_{\alpha\beta}^m[\sin(m\phi_0) \text{ term}], \\ c_{\alpha\beta}^m &= c_{\alpha\beta}^m[\cos(m\phi_0) \text{ term}] + c_{\alpha\beta}^m[\sin(m\phi_0) \text{ term}]. \end{aligned} \quad (D1)$$

Then for moment tensor components $M_{\theta\theta}$, $M_{\phi\phi}$, M_{rr} and $M_{r\theta}$,

$$\begin{aligned} a_{\alpha\beta}^m[\cos(m\phi_0) \text{ term}] &= a_{\alpha\beta}^{-m}[\cos(m\phi_0) \text{ term}], \quad a_{\alpha\beta}^m[\sin(m\phi_0) \text{ term}] = -a_{\alpha\beta}^{-m}[\sin(m\phi_0) \text{ term}], \\ c_{\alpha\beta}^m[\cos(m\phi_0) \text{ term}] &= c_{\alpha\beta}^{-m}[\cos(m\phi_0) \text{ term}], \quad c_{\alpha\beta}^m[\sin(m\phi_0) \text{ term}] = -c_{\alpha\beta}^{-m}[\sin(m\phi_0) \text{ term}], \\ b_{\alpha\beta}^m[\cos(m\phi_0) \text{ term}] &= -b_{\alpha\beta}^{-m}[\cos(m\phi_0) \text{ term}], \quad b_{\alpha\beta}^m[\sin(m\phi_0) \text{ term}] = b_{\alpha\beta}^{-m}[\sin(m\phi_0) \text{ term}]. \end{aligned} \quad (D2)$$

For moment tensor components $M_{\theta\phi}$ and $M_{r\phi}$,

$$\begin{aligned} a_{\alpha\beta}^m[\cos(m\phi_0) \text{ term}] &= -a_{\alpha\beta}^{-m}[\cos(m\phi_0) \text{ term}], \quad a_{\alpha\beta}^m[\sin(m\phi_0) \text{ term}] = a_{\alpha\beta}^{-m}[\sin(m\phi_0) \text{ term}], \\ c_{\alpha\beta}^m[\cos(m\phi_0) \text{ term}] &= -c_{\alpha\beta}^{-m}[\cos(m\phi_0) \text{ term}], \quad c_{\alpha\beta}^m[\sin(m\phi_0) \text{ term}] = c_{\alpha\beta}^{-m}[\sin(m\phi_0) \text{ term}], \\ b_{\alpha\beta}^m[\cos(m\phi_0) \text{ term}] &= b_{\alpha\beta}^{-m}[\cos(m\phi_0) \text{ term}], \quad b_{\alpha\beta}^m[\sin(m\phi_0) \text{ term}] = -b_{\alpha\beta}^{-m}[\sin(m\phi_0) \text{ term}]. \end{aligned} \quad (D3)$$

To implement these symmetries requires the calculation of the expansion coefficients for four separate cases involving the source term of eq. (B6): either of the sets of moment tensor components $\{M_{\theta\theta}, M_{\phi\phi}, M_{rr}, M_{r\theta}\}$ or $\{M_{\theta\phi}, M_{r\phi}\}$ and either of the $\cos(m\phi_0)$ or $\sin(m\phi_0)$ terms. This requires the calculation of only one numerical inverse of the stiffness matrix and multiplication of this inverse with each of four source-term vectors, which adds negligibly to the computation time. Eqs (D2) and (D3), which are also valid for finite sources, allow the computation of the expansion coefficients to be restricted to non-negative m , resulting in a speedup of a factor of 2 in the computation.